Geochemistry, Geophysics, Geosystems®

RESEARCH ARTICLE
10.1029/2024GC011481

Iron Oxyhydroxide-Rich Hydrothermal Deposits at the High-Temperature Fåvne Vent Field, Mohns Ridge

Caroline Gini[1], John W. Jamieson[1], Eoghan P. Reeves[2], Amy Gartman[3], Thibaut Barreyre[4], Michael G. Babechuk[1], Steffen L. Jørgensen[2], and Katleen Robert[5]

[1]Department of Earth Sciences, Memorial University of Newfoundland, St. John's, NL, Canada, [2]Department of Earth Science, Centre for Deep Sea Research, University of Bergen, Bergen, Norway, [3]U.S. Geological Survey, Pacific Coastal and Marine Science Center, Santa Cruz, CA, USA, [4]Geo-Ocean, CNRS-UMR6538, European Institute for Marine Studies, Plouzané, France, [5]School of Ocean Technology, Fisheries and Marine Institute of Memorial University of Newfoundland, St. John's, NL, Canada

Abstract The recently discovered Fåvne vent field, located at 3,040 m depth on the slow-spreading Mohns mid-ocean ridge between Greenland and Norway, is a high-temperature (≥250°C) vent field that is characterized by Fe oxyhydroxide-rich and S-poor chimneys and mounds. The vent field is located on both the hanging wall and footwall of a normal fault with a ∼1.5 km throw that forms the western edge of the ∼20 km wide ridge axial valley. Data collected during exploration of the site using a remotely operated vehicle as well as mineralogical and geochemical analyses of rock samples and sediments are used to characterize the geological setting of the vent field and composition of the hydrothermal deposits. The chimney walls are highly porous and lack defined chalcopyrite lined conduits, typical of high-temperature chimneys. Overall, abundant Fe oxyhydroxide precipitation at high-temperature vents at Fåvne reflects an excess of Fe over reduced S in the fluid, leading to precipitation of Fe oxide and oxyhydroxide minerals at high to moderate temperature vents (>100°C), and as microbially mediated and abiotic precipitation of Fe oxyhydroxide minerals at low-temperature diffuse vents (<100°C). The mounds and chimneys exhibit low base metal and reduced S concentrations relative to globally averaged seafloor deposits and suggest subseafloor mixing of hydrothermal fluid with seawater, causing metal sulfide precipitation. Cobalt enrichment at Fåvne may reflect a subsurface influence of an ultramafic substrate on circulating fluids, although ultramafic rocks are absent on the seafloor and no other elements typical of ultramafic deposits are present.

Plain Language Summary Seafloor hydrothermal deposits are mineral deposits formed from seawater penetrating the oceanic crust and becoming enriched in metals by leaching the surrounding rocks as the temperature rises close to a heat source. Once heated, the fluid rises back to the seafloor where it comes into contact with cold seawater and the metals precipitate, forming chimneys and mounds. The minerals and metal concentrations record temperatures of formation and environments, and can help us understand the processes associated with plate tectonics and the formation of ore deposits. Using underwater vehicles, we collected rocks and sediments from the Fåvne vent field and measured the temperature of the chimneys, mounds, and surrounding seafloor to understand how these deposits form on the seafloor. The Fåvne vent field differs from other vent fields because it is enriched in iron-rich-minerals and depleted in sulfur-rich-minerals. The dominance of iron-rich minerals and the abundance of fractures in the seafloor at the vent field suggest that the hydrothermal fluid is cooled by seawater percolating along the fractures, accumulating these metals in the subsurface instead of at the seafloor. This process is important for understanding the current land-based mineral deposits being mined today and for the exploration of seafloor mineral deposits.

Key Points:

- The Fåvne vent field consists of chimneys and mounds composed of Fe oxyhydroxide minerals with minor sulfide minerals
- Venting of hot fluids with temperatures up to 267°C is dominantly diffuse, sustaining significant microbial communities
- Low base metal concentrations of the Fåvne deposits suggest subsurface seawater mixing and mineral precipitation

Supporting Information:

Supporting Information may be found in the online version of this article.

Correspondence to:

C. Gini,
cgini@mun.ca

Citation:

Gini, C., Jamieson, J. W., Reeves, E. P., Gartman, A., Barreyre, T., Babechuk, M. G., et al. (2024). Iron oxyhydroxide-rich hydrothermal deposits at the high-temperature Fåvne vent field, Mohns Ridge. *Geochemistry, Geophysics, Geosystems*, *25*, e2024GC011481. https://doi.org/10.1029/2024GC011481

Received 2 FEB 2024
Accepted 31 MAY 2024
Corrected 28 JUN 2024

This article was corrected on 28 JUN 2024. See the end of the full text for details.

Author Contributions:

Conceptualization: Caroline Gini, John W. Jamieson, Eoghan P. Reeves, Amy Gartman
Data curation: Caroline Gini
Formal analysis: Caroline Gini
Funding acquisition: John W. Jamieson, Eoghan P. Reeves, Amy Gartman, Thibaut Barreyre, Katleen Robert

1. Introduction

Hydrothermal systems and associated fluid venting at the seafloor are known to occur along all submarine tectonic boundaries (e.g., Beaulieu et al., 2015). The composition of the fluids and associated minerals that accumulate at the vent sites vary depending on a variety of geological controls, including the composition of the host rock, abundance of magmatic volatiles, pH and temperature of the fluids, and depth of venting (e.g., Hannington et al., 2005; Monecke et al., 2016; Von Damm, 1990). High-temperature hydrothermal deposits on mid-ocean ridges (MORs) are typically composed primarily of metal- and sulfide-rich minerals, often forming seafloor massive sulfide (SMS) deposits that are analogous to ancient volcanogenic massive sulfide (VMS) deposits that

Investigation: Caroline Gini, John W. Jamieson, Eoghan P. Reeves, Amy Gartman
Methodology: Caroline Gini
Resources: John W. Jamieson, Eoghan P. Reeves, Amy Gartman, Thibaut Barreyre, Steffen L. Jørgensen
Supervision: John W. Jamieson, Katleen Robert
Validation: Michael G. Babechuk
Visualization: Caroline Gini, John W. Jamieson
Writing – original draft: Caroline Gini, John W. Jamieson, Eoghan P. Reeves, Amy Gartman
Writing – review & editing: Caroline Gini, John W. Jamieson, Eoghan P. Reeves, Amy Gartman, Thibaut Barreyre, Michael G. Babechuk

occur on land (Hannington et al., 2005; Jamieson et al., 2015). At slow-spreading ridges, hydrothermal fluids can interact with deep layers of the oceanic crust through crustal-scale faults that exhume lower crust and/or upper mantle material, such as oceanic core complexes or detachment faults (Escartín et al., 2008; MacLeod et al., 2009; Smith et al., 2006). In these structural settings, the interaction of hydrothermal fluid with lower-crustal rocks typically results in hydrothermal deposits at the seafloor that are characterized by relatively high Au, Cu, Zn, Co, and Ni concentrations (Fouquet et al., 2010). Throughout this paper we use the term "deposit" in the geological sense, which is analogous to precipitates or accumulations, and does not indicate any information about the possible resource potential of such accumulations.

The sulfide minerals that form at hydrothermal vents are stable under reducing conditions but will weather to oxyhydroxide minerals under oxidizing seawater conditions (Edwards, 2004; Gartman & Luther, 2014; Murton et al., 2019; Seyfried & Mottl, 1982). Iron-oxyhydroxide minerals can also occur as primary low-temperature (<100°C) precipitates (Alt, 1988; González et al., 2020; Hekinian et al., 1993) or direct precipitates from Fe-oxidizing microbes (Dekov et al., 2010; Dong et al., 2022; Rouxel et al., 2018), or a combination of all of these processes (Hopkinson et al., 1998). Although Fe oxides and oxyhydroxides are common at low-temperature diffuse vents or coating higher-temperature active and inactive hydrothermal vents, deposits that are dominated by Fe oxyhydroxides formed by direct precipitation from hydrothermal fluid are less common. Examples include Lilliput, on the southern Mid-Atlantic Ridge (MAR; Dekov et al., 2010), Troll Wall, at the Jan Mayen area of Mohns Ridge (Johannessen et al., 2017), and Kama'ehuakanaloa Seamount (previously named Loihi), near Hawaii (Emerson & Moyer, 2002; Hekinian et al., 1993). The formation of low-temperature Fe-Si precipitates has also been documented in association with Proterozoic VMS settings and investigated with respect to abiotic and microbial processes and seawater chemistry in the Proterozoic eon (Dong et al., 2022; Little et al., 2021; Slack et al., 2007, 2009).

The Fåvne vent field located at 72.7°N and 3.8°E on the Mohns Ridge in the Norwegian and Greenland Seas (Figure 1) was discovered and mapped in 2018 by the Norwegian Petroleum Directorate (now Norwegian Offshore Directorate) during a regional mapping and sampling program (Norwegian Petroleum Directorate, 2019; Stenløkk et al., 2019). A study by Sahlström et al. (2023) of nine hydrothermal rock samples collected at Fåvne documented elevated concentrations of Co (average: 0.3 wt. %) from chimney fragment samples collected from high-temperature vents, which the authors tentatively link to high salinity fluids and possible interaction with ultramafic rocks. Here, we provide a detailed geological characterization of the Fåvne vent field, a high-temperature vent field dominated by metal-poor, Fe oxyhydroxide-rich chimneys and mounds located at the base of an axial valley bounding fault. We use a combination of bathymetric mapping, seafloor observations, and mineralogical and geochemical analyses to link vent field composition and morphologies to a highly permeable, faulted and fractured basement associated with the fault that allows for significant subseafloor fluid mixing. We discuss the implications of subseafloor mixing with respect to the formation of modern SMS and ancient VMS deposits.

2. Geological Setting

The Fåvne vent field is located at a depth of ∼3,040 m below sea level on the slow-spreading (15 mm/year) Mohns Ridge (Géli et al., 1994), which extends north-northeast from Jan Mayen to where it intersects the southern termination of the Knipovich Ridge (Figure 1a). The Mohns Ridge is characterized by a 30° obliquity between axial volcanic ridges (AVR), emplaced orthogonally to the current spreading direction, and the ridge valley axis (Figure 1a). This obliquity is attributed to a change in the spreading direction that occurred ca. 33 Ma ago from 160° to 110° (Peyve, 2009). The crust beneath the Mohns Ridge axis near Fåvne is 1–2 km thinner than the typical crustal thickness of ∼6 km along the MAR to the south (Chen, 1992; Klingelhofer et al., 2000). The axial valley of the segment that hosts Fåvne contains an AVR with numerous flat-topped volcanoes that occur mainly on its eastern flank (Figure 1b).

At least seven confirmed or inferred (from detection of hydrothermal plumes in the water column) vent fields have been discovered along the Mohns ridge, corresponding to an along-axis distribution of ∼1 field per 80 km of ridge (Figure 1a; Beaulieu & Szafrański, 2020; Pedersen et al., 2010; Stensland et al., 2019). Hydrothermal systems along the ridge are commonly associated with AVRs and are located either directly on the AVR or on its flanks (e.g., Loki's Castle, Soria Moria) or on low-angle fault walls (e.g., Mohn's Treasure, Copper Hill; Pedersen et al., 2010). By contrast, Fåvne is located on the axial valley floor, at the base of a normal fault with a ∼1.5 km

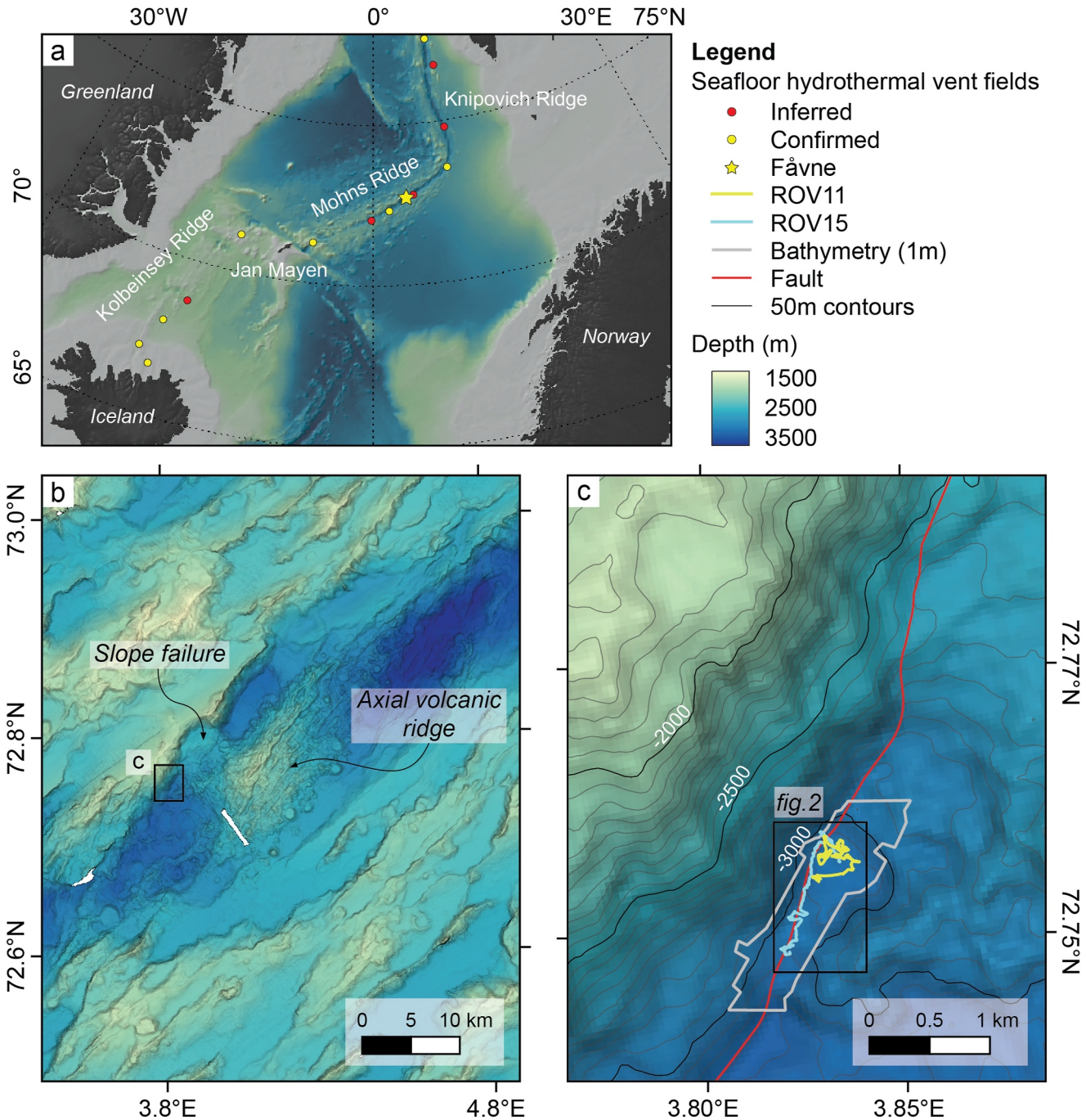

Figure 1. (a) Location of the Fåvne vent field and other confirmed and inferred hydrothermal vent fields within the Norwegian and Greenland Seas (Beaulieu & Szafrański, 2020; Bohrmann, 2022). (b) Regional setting of the ridge segment hosting the Fåvne vent field on the Mohns Ridge. Ship-based bathymetry, 50 m resolution, from the Norwegian Mapping Authority (2019). (c) Outline of the highresolution bathymetric map (1 m resolution; Norwegian Petroleum Directorate, 2019) and dive tracks of the two remotely operated vehicle (ROV) dives that explored the Fåvne vent field at the base of a major fault scarp bounding the axial valley.

throw that forms the western boundary of the valley (Figure 1c). A large valley wall slope failure occurs directly north of the vent field (Figure 1b). An additional site of sulfide mineralization, named Gnitahei, occurs ~700 m SW of Fåvne (Brekke et al., 2021). This site occurs solely on the scarp and, to date, no hydrothermal activity has been reported there (Sahlström et al., 2023).

3. Methods

3.1. Vent Field Exploration and Sampling

Data for this study, consisting of visual surveys, temperature measurements, and rocks and sediment core sampling, were collected using the remotely operated vehicle (ROV) *Ægir6000* (University of Bergen, Norway) operated from the Norwegian research vessel *G.O. Sars* during a 2019 research expedition led by the Center for Deep Sea Research at the University of Bergen. The ROV's position on the seafloor was determined using a high precision acoustic positioning ultra-short baseline system that yielded a positional accuracy of 5–20 m. Two dives were dedicated to exploration and rock sampling covering 4.8 km of seafloor during ~18 hr of bottom time (Figure 2). Additional dives allowed temperature measurements and push core sampling. Exploration was partly guided by previously collected autonomous underwater vehicle-based high resolution (1 m) bathymetric data (Norwegian Petroleum Directorate, 2019). Together, the visual exploration and bathymetric data were used to create a geological map of the Fåvne vent field (Figure 3).

For this study, 25 rock samples were collected from active and inactive hydrothermal mounds, chimneys, and talus. Four sediment push cores were also collected from sedimented areas within the vent field (Figure 2). Temperature was measured within sediments and hydrothermal structures at over 30 locations with a temperature probe (EP Oceanographic 1010 Hi-T Data Logger, Woods Hole Oceanographic Institution, Woods Hole, U.S.A.; WHOI) that provided ±0.6°C accuracy and 0.03°C resolution. Focused vent temperatures were also measured at four areas of focused hydrothermal venting using isobaric gas-tight (IGT) fluid samplers (±2°C uncertainty; Figure 2; Table S1; Seewald et al., 2002). The IGT temperatures were reproducible within a few degrees between duplicate samplers, and the values reported reflect the stable maxima in the associated vent orifices. A list of samples, sample locations, and temperatures is available in Table S1.

3.2. Rock Sample Analysis

3.2.1. Mineralogy of the Hydrothermal Structures

Hydrothermal rock samples collected during ROV dives were grouped into sulfide-rich (n = 14, this group is dominated by sulfide-rich samples but also includes 2 sulfate-rich samples) or Fe oxyhydroxide-rich (n = 11) based on visual assessment at the time of collection. After collection, the sulfide-rich samples were rinsed with fresh water to remove salts, but the highly friable Fe oxyhydroxide-rich samples were not rinsed to prevent their disintegration. Thin sections of sulfide-rich samples with sufficient material (n = 11) were made in the Department of Earth Sciences at Memorial University of Newfoundland (St John's, Canada). The Fe oxyhydroxide-rich samples were too friable to make thin sections. Mineralogy and associated modal abundances of the sulfide-rich samples were determined through reflected and transmitted light optical microscopy, scanning electron microscopy (SEM), and electron probe micro-analysis (EPMA). For SEM analysis, a JEOL JSM 7100F field emission SEM with an energy dispersive spectrometer in the TERRA facility at Memorial University was used, with an accelerating voltage of 15 kV. A JEOL JXA 8230 EPMA with energy dispersive X-ray spectroscopy, also in the TERRA facility, was used for mineral-specific trace element analysis, with a tungsten source accelerating the electron beam at 20 kV and a resolution of 20 nA. X-ray diffraction (XRD), using a Rigaku Ultima-IV XRD with Cu source, monochromator and scintillation detector, operated at an acceleration voltage of 40 kV and a current of 44 mA, was used to identify minerals in the Fe oxyhydroxide-rich samples. The XRD scan range was from 3 to 100° 2θ, with a scan rate of 0.02° per second. A side packed aluminum mount was used to minimize preferred mineral orientation. Spectral interpretation was aided by the International Center for Diffraction Data database in the JADE software (Gates-Rector & Blandon, 2019).

3.2.2. Bulk Composition of Rock Samples

Bulk analyses for major and trace element concentrations were carried out at Actlabs (Ancaster, Ontario, Canada). Samples were crushed using a steel mill and pulverized to a powder size of <105 µm (Actlab code RX1). Fourteen sulfide-rich samples were prepared with Na_2O_2 fusion followed by analysis using inductively coupled plasma-mass spectrometry (ICP-MS) and -optical emission spectroscopy (-OES; Actlabs code Ultratrace 7). The sulfide-rich samples were also analyzed by instrumental neutron activation analysis (INAA, Actlabs code 1D Enhanced). When both methods (INAA and fusion ICP-MS/OES) were used to analyze an element, the analysis with the lower detection limit was selected. The 11 Fe oxyhydroxide-rich samples were prepared using a $LiBO_2$/

10.1029/2024GC011481

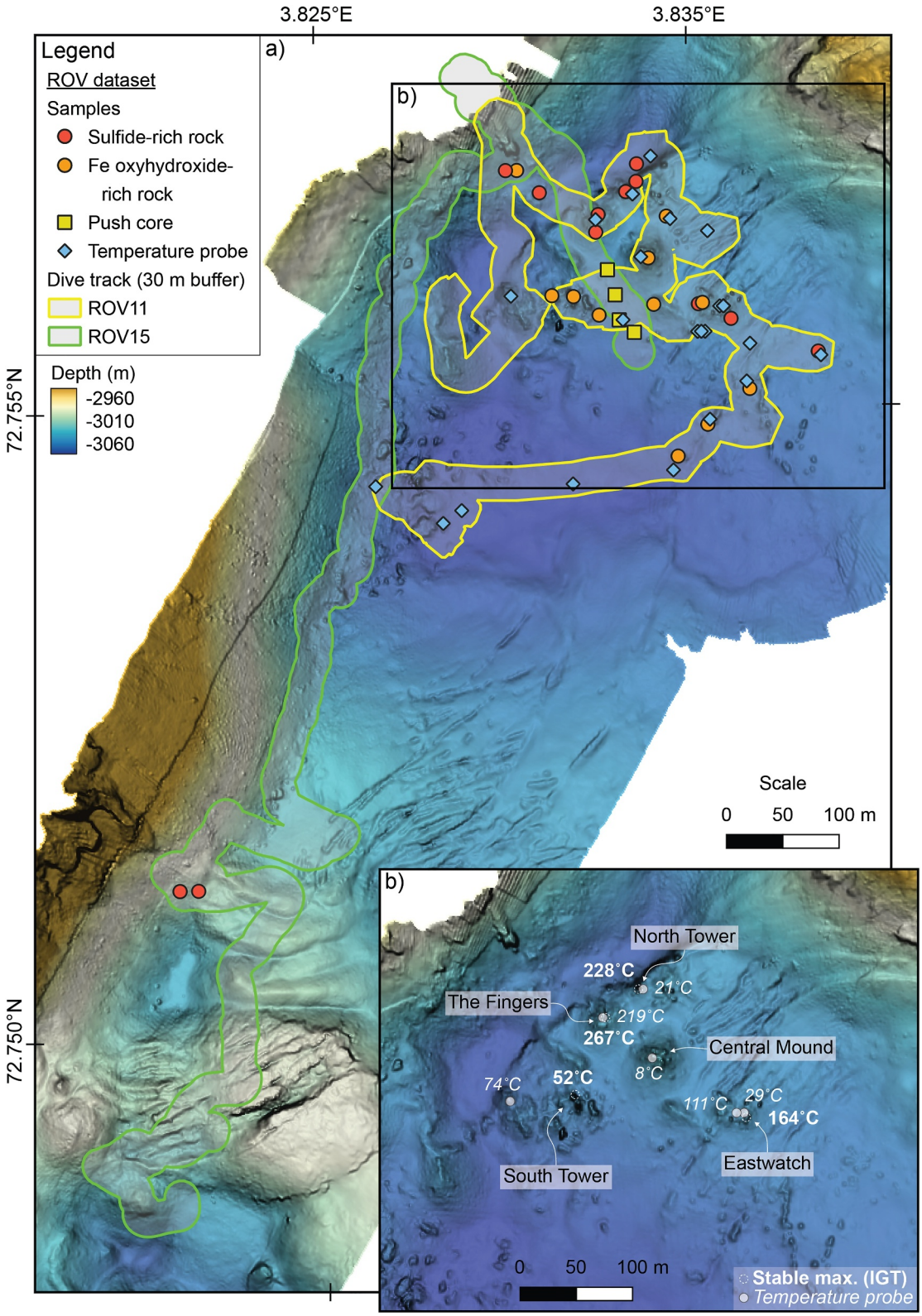

Figure 2. Bathymetric map (1 m resolution; Norwegian Petroleum Directorate, 2019) of the Fåvne vent field and surrounding area. (a) Remotely operated vehicle dive tracks and locations of rock samples, push cores, and temperature probe measurements. (b) Named vent complexes within the Fåvne vent field and temperatures recorded above ambient seawater temperatures (~−0.7°C), using the isobaric gas-tight sampler at vent orifices (bold) and the temperature probe on mounds (italics).

$Li_2B_4O_7$ fusion and analyzed by ICP-MS and -OES (Actlabs code 4Litho). The full bulk geochemistry results with analytical methods and detection limit used for each element are included in Table S2.

A randomly selected sulfide-rich sample was used for duplicate ICP analysis with all elements reproducing within 10% except for Ga (13%), In (20%), and Se (15%). The Actlabs selected reference materials measured by INAA ($n = 3$) and Na_2O_2 fusion ICP-MS/OES ($n = 16$) included concentrations similar to the range of the sulfide-rich samples. The Actlabs selected reference materials measured by $LiBO_2/Li_2B_4O_7$ fusion ICP-MS and -OES ($n = 13$) exhibited concentrations higher than the range of concentration in the Fe oxyhydroxide-rich samples. All quality control data, including an assessment of accuracy using a percent bias calculation for all reference materials measured by Actlabs for this study are available in Table S3.

3.3. Push Cores

Four push cores were collected along a transect within 10–30 m of inactive mounds and 30–100 m of active venting (Figure 2). After collection, the cores were refrigerated, scanned with a Geotek rotating X-ray computed tomography (RXCT), split, photographed, and subsampled for XRD and geochemical analyses. The locations of subsampled layers within each core are available in Figure S1 of the Supporting Information S1. Mineral identification was completed by XRD analysis using a X'Pert3 powder diffractometer by Malvern Panalytical at the U.S. Geological Survey Pacific Coastal and Marine Science Center (Santa Cruz, U.S.A.), with a scan range from 5 to 70° 2θ. The final spectra represent an average of scans performed at 0, −1 and +1° wobble. The subsamples were categorized into "contains sulfide minerals" or "without sulfide minerals" based on the presence or absence of sulfide minerals determined via visual identification and XRD (Figures S1 and S2 in Supporting Information S1). Bulk geochemical analyses of sediment subsamples were performed by ICP-MS, ICP-atomic emission spectroscopy (AES), X-ray fluorescence (XRF), and INAA at SGS Laboratories (Mississauga, Canada). See Gartman et al. (2024) for the full data set and description of analytical methods.

Three radiocarbon ages were obtained from discrete intervals from two of the push cores. Organic carbon was analyzed for $\delta^{13}C$ and $\Delta^{14}C$ at the National Ocean Sciences Accelerator Mass Spectrometry facility at WHOI. Samples were combusted to graphite using a furnace followed by analysis using a continuous flow accelerator mass spectrometry system. NBS Oxalic Acid I (NIST-SRM-4990) was used as the primary standard for ^{14}C. Reported ages (Table S4) are calculated after Stuiver and Polach (1977) and Stuiver (1980).

4. Results

4.1. Geology of the Fåvne Vent Field

The Fåvne vent field is spatially associated with two major tectonic structures: the major east-dipping normal fault with a ∼1.5 km throw that bounds the western edge of the axial valley, hereafter referred to as the main fault, and a secondary, smaller antithetic west-dipping normal fault extending ∼200 m along the main fault with a 5–10 m throw (Figures 3 and 4). The two faults define a ∼40 m wide graben. The valley floor that hosts the vent field consists of intact and broken pillow lavas that are variably overlain by relatively thin (∼1 m thick) sediments (Figure 5a). Hydrothermal deposits occur both on the hanging wall and footwall of both faults and cover a 300 × 400 m area (Figures 3 and 4). The deposits on the axial valley floor consist of sub-circular hydrothermal mounds, each hosting several active and/or inactive chimneys. Here, the seafloor is relatively flat, fissured in places, and variably covered by maximum 1 m thick sediments. West of this main cluster, hydrothermal crusts and steep edifices topped with inactive chimneys also occur within the graben and extend at least 100 m upslope on the scarp surface (Figures 3 and 4). Orange and green hydrothermal talus mixed with broken pillows occurs on the fault scarp 600 m south of the main vent field. This hydrothermal debris talus is located directly downslope from the inactive Gnitahei site, which, at the time of the expedition, had not yet been discovered (Figures 3a and 5b; Brekke et al., 2021).

4.1.1. Basement Geology

The axial valley floor is dominated by sediments (Figure 5c). Numerous fissures throughout the valley floor expose pillow basalts directly beneath the sediments. Pillow basalts are also exposed by the secondary fault (Figure 5d). Massive basalt flows with columnar joints are exposed on the fault scarp north-west of the vent field. A volcanic mound to the south of the vent field is composed of faulted and fissured elongated pillows (Figures 3a

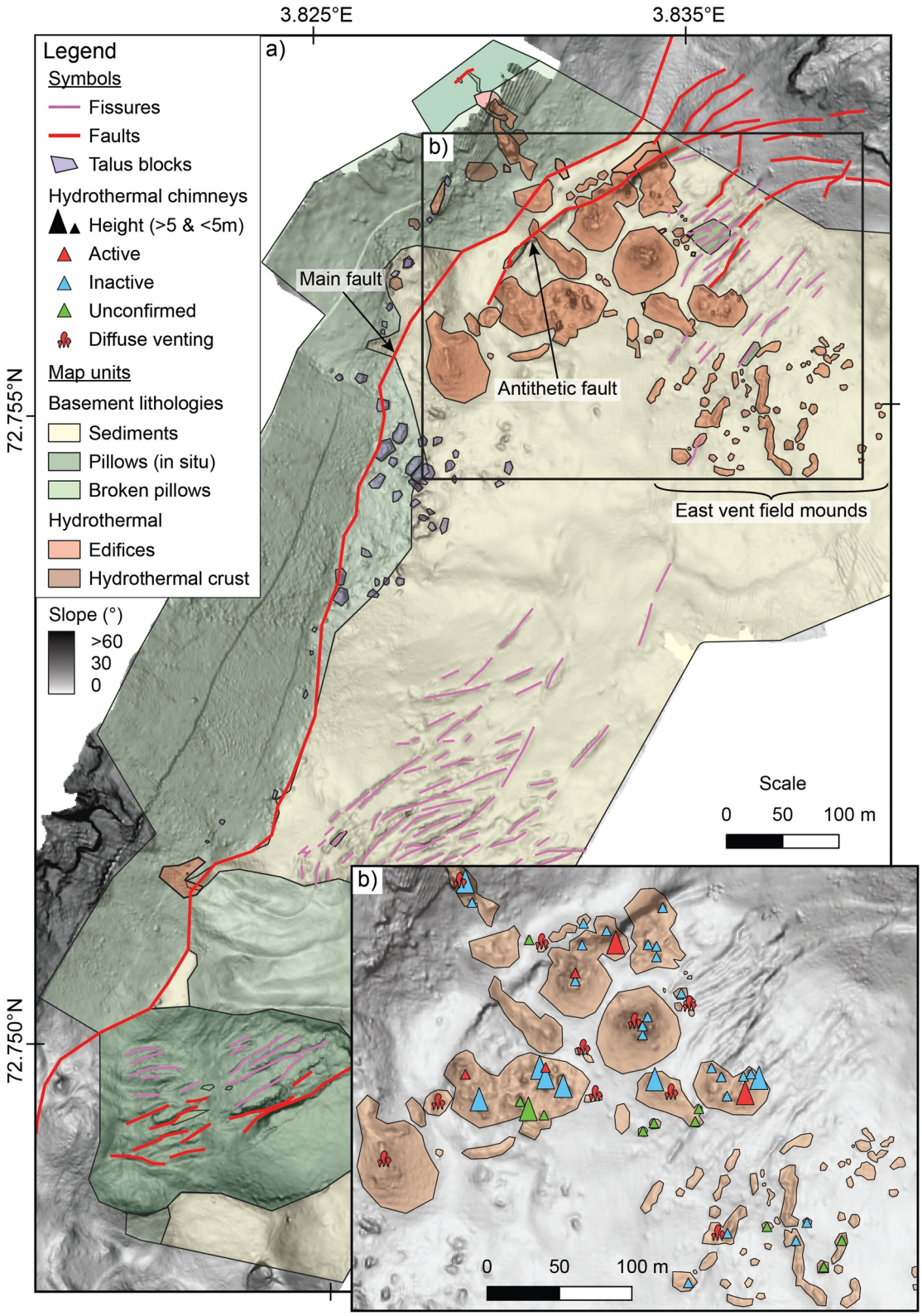

Figure 3. (a) Geological map of the Fåvne vent field, on the slope map derived from the Norwegian Petroleum Directorate (2019) bathymetry. (b) Detailed map of the hydrothermal activity. Triangles represent chimneys >2 m high identified from the bathymetry (green triangles) and visually confirmed (blue and red). Focused venting (black smoker or shimmering fluid) corresponds to active chimneys (red triangles), absence of venting corresponds to confirmed inactive chimneys (blue), and diffuse venting (red plumes) is reported for structures with microbial mats that lack focused venting.

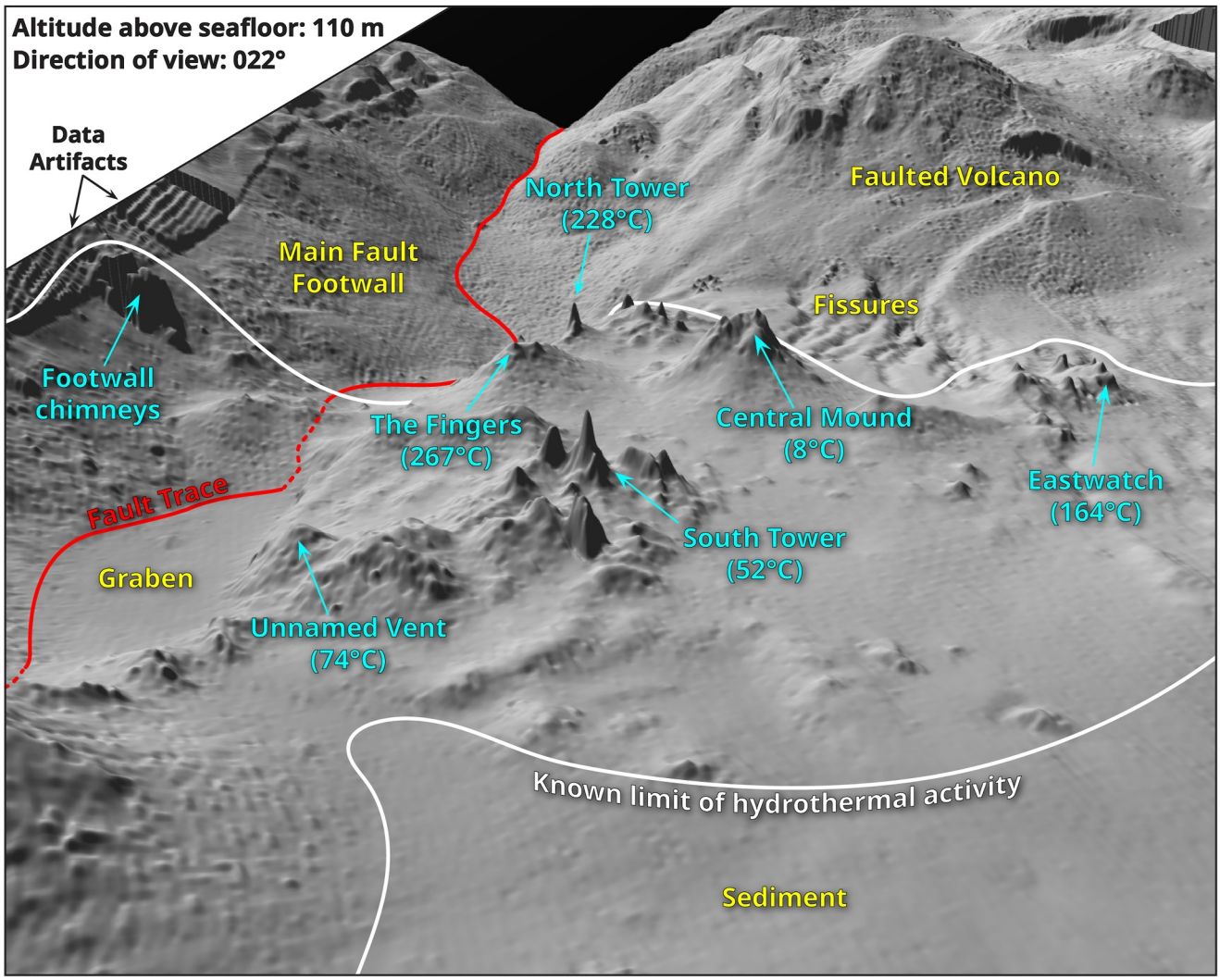

Figure 4. View of the main hydrothermal structures at Fåvne showing locations of elevated fluid temperature measurements and prominent geological features.

and 5e). Overall, the fissures and faults occur both parallel to the average regional strike of the main fault (NNE) and to the strike of the secondary antithetic fault (ENE). The occurrence of pillows on top of sediments within the vent field and minimal sediment accumulation on the volcanic mound (Figure 3) indicate recent volcanic activity in this area.

The base of the fault scarp is covered by broken pillow talus with block sizes of up to 5 m (Figure 5f). Basalt blocks with sizes of up to 50 m occur south of the vent field (Figure 5g). Hydrothermally cemented breccias with angular to subrounded basalt clasts occur within the region of hydrothermal deposits on the fault scarp west of the main vent field.

4.1.2. Hydrothermal Deposits

The deposits within the main area of the hydrothermal vent field consist of individual or coalesced mounds that range from 5–40 m in diameter and 1–20 m high, and standalone chimneys up to 15 m high (Figure 3). The mounds are often topped by clusters of 1–5 m high and 0.5–3 m wide chimneys (Figures 5h–5j). Broken chimney pieces have accumulated at the base of most mounds. The largest mounds and chimneys occur in the western half of the vent field. The eastern half of the vent field is characterized by a series of relatively small (<5 m tall) mounds that are aligned along fissures and have characteristic highly irregular surface morphologies (Figures 3 and 5h). On the fault scarp, hydrothermal deposition consists of a steep-sided edifice topped by a ∼5 m high

10.1029/2024GC011481

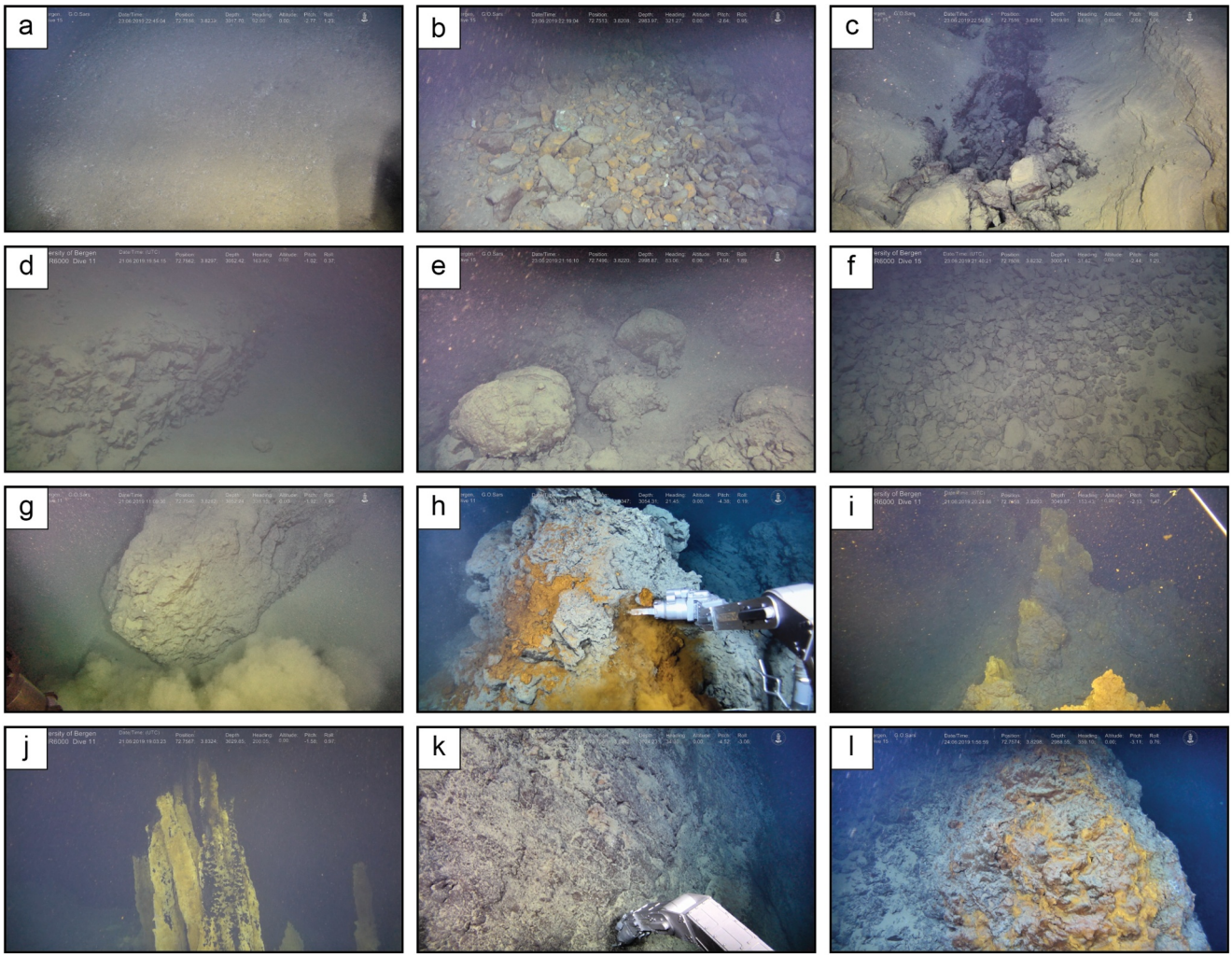

Figure 5. Representative remotely operated vehicle screengrabs of basement lithologies and hydrothermal deposit features. (a) Homogeneous, featureless sedimented seafloor, field of view ∼3 m. (b) Broken pillow talus mixed with orange and green hydrothermally altered material on the fault scarp downslope of Gnitahei, field of view ∼10 m. (c) Fissure on the valley floor exposing pillow basalt beneath ∼1 m of sediment. (d) Two-meter-high secondary fault exposing truncated pillows. (e) Lightly sedimented pillow lavas, each ∼1–2 m wide, on volcanic mound, south of the vent field. (f) Talus of meter-sized blocks of broken pillows on the fault surface, field of view ∼10 m. (g) Large block on the valley floor displaying elongated pillows, field of view ∼8 m. (h) Small, ∼1 m high, Fe oxyhydroxide-rich hydrothermal mound, field of view ∼2 m. (i) Inactive chimneys, <1 m high, at the summit of a hydrothermal mound, field of view ∼10 m. (j) The Fingers, tall black smoker hydrothermal chimney cluster covered by microbial mats, field of view ∼8 m. (k) Indurated hydrothermal crust at the base of the fault scarp within the vent field, vertical field of view ∼2 m. (l) Hydrothermally cemented pillow breccia with yellow microbial mats, field of view ∼5 m.

chimney, hydrothermal crusts (Figure 5k), and hydrothermally cemented basalt breccia (Figure 5l). The occurrence of hydrothermal material on the fault scarp extends upslope until it ends abruptly at the contact between broken pillows and in situ massive basalt flows (Figure 3).

The mounds and chimneys show a range of hydrothermal activity. Focused venting is limited to four areas of stand-alone or clustered chimney structures, mostly in the western half of the vent field, that range from 52°C, relatively clear fluid (South Tower vent), to 267°C "black smoker" style venting (The Fingers vent; Figures 4 and 5j). Stable maximum measured temperatures were determined at only one vent in each of these four areas (Figure 2). Since some of these areas host several venting orifices, these temperatures might not necessarily represent true absolute maxima. However, our sampling campaign attempted to target the most vigorously venting orifices evident in a given area, and we do not expect substantially higher temperatures to be measurable at Fåvne (Figure 4). Significant diffuse venting through the flanks of the higher temperature structures and a lack of discernible primary central fluid conduits at the tops of chimneys indicate a very high degree of fluid permeability through the chimney walls. Widespread lower temperature diffuse venting (below 20°C but above

ambient seawater temperature of −0.7°C) occurs on hydrothermal structures throughout the western half of the vent field. This style of venting is not readily visible from ROV video and was either confirmed from temperature probe measurements or inferred from the presence of yellow microbial mats on the surfaces of hydrothermal mounds and chimneys (Figures 2, 5i, and 5l, Table S1). The lack of both microbial mats and temperature measurements above ambient seawater indicates that the visually surveyed small mounds in the eastern half of the vent field are likely inactive. Microbial mats occur on the deposits on the fault scarp, but higher temperature fluid discharge was not observed. Temperatures measured in sediments ranged between −0.6 (near ambient) and 0.0°C ($n = 17$, Table S1). The hydrothermal activity status of edifices that were not surveyed by ROV but inferred from the high-resolution bathymetry is unknown (Figure 3b). Overall, however, hydrothermal activity at Fåvne is generally dominated by extensive diffuse and some focused low-temperature venting and only limited focused higher-temperature "smoker" venting, the latter having relatively moderate temperatures (228–267°C).

4.2. Mineralogy of the Hydrothermal Deposits

4.2.1. Rock Samples

From the ROV video surveys, the composition of the mounds and chimneys appears to be dominated by orange Fe oxyhydroxide minerals. Sampling of these structures, however, resulted in the recovery of both Fe oxyhydroxide-dominated and also sulfide- (sulfate-) dominated samples (Figures 6a and 6b). Sulfide minerals are generally restricted to the interior of structures, while Fe oxyhydroxide-rich minerals occur throughout both the interiors and exteriors of the structures (Figure 6b). The Fe oxyhydroxide-rich samples are composed of poorly crystalline yellow-orange-red Fe oxyhydroxide minerals, as observed by the broad peaks in the XRD diffractograms (Figure S3 in Supporting Information S1), with very high porosity (visually estimated at up to 50%) and a dusty consistency (Figure 6a). Major minerals include goethite, ferrihydrite (2-line), lepidocrocite, and minor phases of silica, birnessite, clays, and rare disseminated sulfide minerals (sphalerite, pyrite; Table 1). The mounds are generally dominated by ferrihydrite, whereas the chimneys are dominantly composed of goethite. Samples with abundant ferrihydrite normally comprise sub-mm-sized filaments oriented perpendicularly to the exterior surface of the samples (Figure 6c). Generally, the exteriors of the samples from both chimneys and mounds are composed of Mn- and Fe oxyhydroxides and rare disseminated pyrite, forming crusts that occasionally contain mm- to cm-wide conduits. Chimneys with abundant Fe oxyhydroxide minerals also contain transparent amorphous Si forming up to 2 mm-thick layers parallel to the exterior crust (Figure 6c).

Samples collected from the actively venting high-temperature chimneys (>150°C) are primarily composed of anhydrite, pyrrhotite, sphalerite, and chalcopyrite, with minor isocubanite, pyrite, magnetite, and Fe oxyhydroxide minerals (Figures 6d and 6e, Table 1). Orange Fe oxyhydroxide minerals (dominantly goethite) cover the sample exteriors and, for some samples, line pore spaces in the sample interiors (Figure 6b). The sulfide-rich samples have high porosity due to the many mm- to cm-scale conduits (visually estimated in thin section as 20%–40%) that lack a defined chalcopyrite lining. Two samples, one collected from an active chimney and one from an inactive chimney, are dominantly composed of magnetite and Fe oxyhydroxide minerals, with a lesser abundance of sulfide minerals (Figures 6e–6g).

In contrast to the active chimneys, the inactive sulfide-rich samples lack anhydrite, most likely due to the retrograde solubility of anhydrite in seawater at temperatures <150°C (Humphris et al., 1995), and contain a greater abundance of amorphous silica, sphalerite-würtzite, and Fe oxyhydroxides, with lower amounts of pyrrhotite, chalcopyrite, and magnetite (Figures 6h and 6i; Table 1). Rare galena was identified in one sample (Figure 6j). Iron-oxyhydroxide minerals occur as colloform layers on the exterior of the structures, as spherules associated with silica, and as oxidative replacement products of pyrrhotite (Figures 6b, 6g, and 6h). On the fault scarp, a sulfide-rich and an Fe oxyhydroxide-rich samples were collected at the base of an inactive chimney. The sulfide-rich sample has a similar mineralogy to samples collected at the base of active, high-temperature chimneys, except for the presence of host rock clasts and a high degree of pyrrhotite oxidation (GS19–ROV15–R11, Figure 6k). The Fe oxyhydroxide-rich sample contains traces of atacamite on its exterior.

The mounds in the eastern area are dominated by Fe oxyhydroxide minerals (primarily ferrihydrite) with only trace abundance of sulfide minerals. Here, it is unclear whether these morphologically distinct mounds are dominantly composed of Fe oxyhydroxide minerals or the Fe oxyhydroxide minerals occur as an especially thick exterior coating of a sulfide-rich interior. Easy penetration of the ROV robotic arm into one of the mounds suggests that the Fe oxyhydroxide-rich exterior layer is at least 15 cm thick.

Geochemistry, Geophysics, Geosystems

10.1029/2024GC011481

Table 1
Mineralogy of the Fåvne Hydrothermal Deposits Determined by Transmitted Light Optical Microscopy (Sulfide/Sulfate-Rich Samples) and by XRD (Fe Oxyhydroxide-Rich Samples and Push Core Sediments)

Location	Sample name	Structure	Description	Mineral abundance		
				Major (>25%)	Moderate	Minor (<5%)
Rocks						
Main vent field area, The Fingers	GS19_ROV14_R05	Active chimney, focused	Sulfide-rich	magnetite, Fe oxyhydroxides	pyrrhotite, anhydrite	sphalerite, pyrite
Main vent field area, North Tower	GS19_ROV16_R02	Active chimney, focused	Sulfide-rich	anhydrite, sphalerite	pyrrhotite, isocubanite, chalcopyrite	Fe oxyhydroxides, magnetite
Main vent field area, Eastwatch	GS19_ROV14_R04	Active chimney, focused	Sulfide-rich	anhydrite, pyrrhotite	chalcopyrite, isocubanite, sphalerite	Fe oxyhydroxides, pyrite
Main vent field area, South Tower	GS19_ROV16_R01	Active chimney, focused	Fe oxyhydroxide-rich	ferrihydrite	–	–
Main vent field area, The Fingers	GS19_ROV11_R17	Base of active chimney, focused	Sulfide-rich	n.a.	n.a.	n.a.
Main vent field area, North Tower	GS19_ROV11_R15	Base of active chimney, focused	Sulfide-rich	n.a.	n.a.	n.a.
Main vent field area, North Tower	GS19_ROV11_R16	Base of active chimney, focused	Sulfide-rich	amorphous silica, sphalerite	pyrrhotite	chalcopyrite, Fe oxyhydroxides, pyrite
Main vent field area, North Tower	GS19_ROV11_R14	Base of active chimney, focused	Sulfide-rich	amorphous silica	sphalerite, Fe oxyhydroxides	pyrrhotite, isocubanite, chalcopyrite
Main vent field area, Central Mound	GS19_ROV11_R12	Active chimney, diffuse	Fe oxyhydroxide-rich	goethite, ferrihydrite	lepidocrocite	clay, birnessite
Main vent field area, South Tower	GS19_ROV11_R10	Active mound, diffuse	Fe oxyhydroxide-rich	ferrihydrite	halloysite	lepidocrocite, birnessite
Main vent field area, Eastwatch	GS19_ROV11_R07	Inactive chimney	Sulfide-rich	magnetite	pyrite, Fe oxyhydroxides	sphalerite
Main vent field area, South Tower	GS19_ROV11_R11	Inactive chimney	Fe oxyhydroxide-rich	goethite	lepidocrocite, ferrihydrite	–
Main vent field area, Eastwatch	GS19_ROV11_R08	Inactive chimney	Fe oxyhydroxide-rich	ferrihydrite	opal	–
Main vent field area	GS19_ROV11_R09	Inactive mound	Fe oxyhydroxide-rich	goethite	ferrihydrite	lepidocrocite
Main vent field area	GS19_ROV11_R13	Inactive mound	Fe oxyhydroxide-rich	clay	ferrihydrite, opal	lepidocrocite
Eastern vent field area	GS19_ROV11_R03	Active mound, diffuse	Fe oxyhydroxide-rich	ferrihydrite	birnessite	halloysite
Eastern vent field area	GS19_ROV11_R02	Inactive mound	Fe oxyhydroxide-rich	goethite	ferrihydrite	clay, birnessite
Eastern vent field area	GS19_ROV11_R04	Inactive mound	Fe oxyhydroxide-rich	ferrihydrite	sphalerite	–
Eastern vent field area	GS19_ROV11_R05	Inactive mound	Sulfide-rich	n.a.	n.a.	n.a.
Fault scarp area	GS19_ROV15_R10	Base of active chimney, diffuse	Fe oxyhydroxide-rich	goethite, lepidocrocite	ferrihydrite	clay, atacamite
Fault scarp area	GS19_ROV15_R11	Base of active chimney, diffuse	Sulfide-rich	pyrrhotite	sphalerite, isocubanite, chalcopyrite	Fe oxyhydroxides, host rock clasts
Fault scarp area	GS19_ROV11_R18	Inactive mound	Sulfide-rich	pyrrhotite, sphalerite	Fe oxyhydroxides	chalcopyrite, pyrite, galena

Geochemistry, Geophysics, Geosystems

10.1029/2024GC011481

Table 1
Continued

Location	Sample name	Structure	Description	Mineral abundance		
				Major (>25%)	Moderate	Minor (<5%)
Gnitahei	GS19_ROV15_R02	Talus	Sulfide-rich	pyrite	marcasite	sphalerite, chalcopyrite
Gnitahei	GS19_ROV15_R03	Talus	Sulfide-rich	pyrite, marcasite	–	chalcopyrite
Gnitahei	GS19_ROV15_R04	Talus	Sulfide-rich	pyrite	host rock clasts, Fe oxyhydroxides	–
Sediments		**Depth interval**				
Main vent field area	ROV12_PC02	3.5–9	Without sulfide	ferrihydrite	opal	quartz
	Max 24 cm	12.5–16	Without sulfide	goethite, chlorite	albite, ferrihydrite	quartz, birnessite, halite
		16–19.5	Without sulfide	goethite	chlorite, ferrihydrite	albite, birnessite, quartz, halite
Main vent field area	ROV17_PC01	0–5	Without sulfide	chlorite, albite	goethite, ferrhydrite	quartz, birnessite, halite
	Max 16 cm	10.5–12.5	With sulfide	goethite	lepidocrocite	pyrrhotite, chalcopyrite, halite
		12.5–13.5	With sulfide	goethite	lepidocrocite, pyrrhotite	chalcopyrite, sphalerite, halite
Main vent field area	ROV17_PC02	6.5–10	Without sulfide	goethite	chlorite, ferrihydrite	quartz
	Max 31 cm	20.5–22.5	With sulfide	goethite	chalcopyrite	quartz, chlorite, halite
		25.5–28.5	With sulfide	goethite	halite, chlorite	chalcopyrite, quartz
Main vent field area	ROV17_PC03	15.5–18.5	Without sulfide	chlorite	ferrihydrite, albite, goethite	illite, quartz, birnessite
	Max 25 cm	18.5–20	Without sulfide	chlorite	chlorite, goethite, ferrihydrite, albite	illite, quartz, halite
		24.5–25	Without sulfide	chlorite	ferrihydrite, albite, goethite	quartz, halite

Note. Not analyzed: n.a; no value: –.

10.1029/2024GC011481

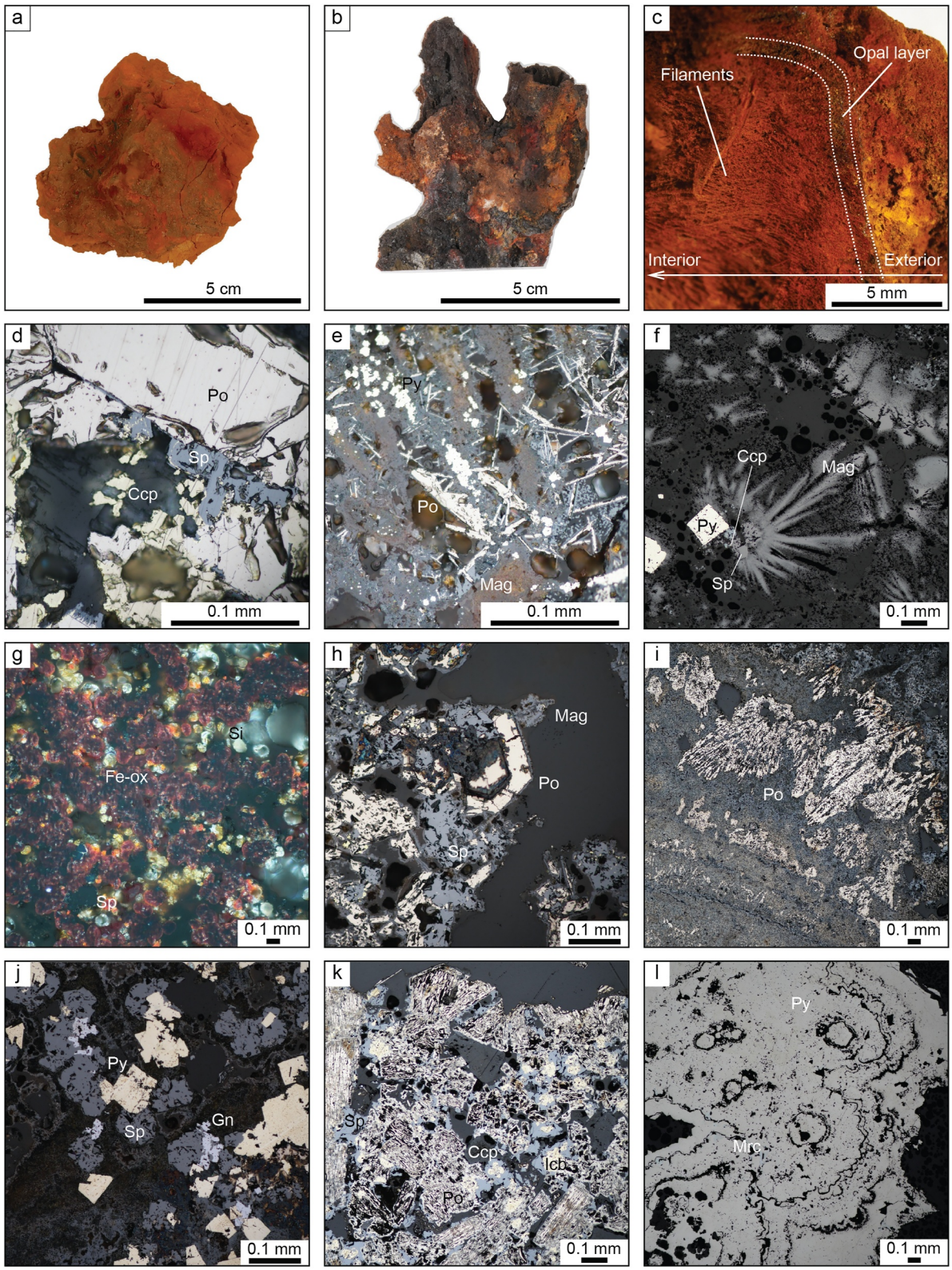

Figure 6.

The three sulfide-rich samples collected from the talus on the fault scarp, downslope of Gnitahei, are pervasively altered mafic rocks. The alteration is dominated by a stockwork vein network of pyrite and marcasite, with total sulfide mineral abundance exceeding 80% (Figure 6l). In addition to the high pyrite and marcasite abundances, notable differences between these samples and those from Fåvne include rare gold inclusions in the pyrite, significant atacamite on the sample exteriors, and only a thin layer of Fe oxyhydroxide mineralization on the sample exteriors (Figure 6l and Figure S4 in Supporting Information S1).

4.2.2. Push Core Sediments

Between 16 and 31 cm of the uppermost layers of sediments were recovered from the four sediment push cores within the main vent field area. Overall, the mineralogy of the sediments is dominated by goethite, lepidocrocite, ferrihydrite, chlorite, and albite (Table 1). Ferrihydrite is the dominant mineral at the surface and more crystalline goethite increases in abundance below 5–10 cm, suggesting recrystallization of ferrihydrite to goethite at depth (Figure S2 in Supporting Information S1). Cores GS19–ROV17–PC01 and –PC02 contain layers of sulfide minerals interlayered with the oxyhydroxide minerals at depth within the cores. The multi-cm thick coherent regions characterizing the cores and associated CT scans (Gartman et al., 2024) suggest that most of the sediment in the cores were accreted by mass-wasting processes, as opposed to deposition of hemipelagic sediments. Exceptions to this method of accretion include the interval between 19 and 28 cm of core GS19–ROV17–PC02, which exhibits sub-cm fine-grained laminations suggesting plume fallout, and core GS19–ROV17–PC03 contains a component of pelagic material and has a series of seven layers of coarse volcanic glass winnowing to fine-grained clay between 11.5 and 15 cm depth, interpreted to indicate an eruption sequence (Figure S1 in Supporting Information S1). Birnessite (Mn oxide) appears in the surface layer of GS19–ROV17–PC01 but only in the deeper layers of GS19–ROV12–PC02 and GS19–ROV17–PC03 (Figure S2 in Supporting Information S1). There is a lack of correlative stratigraphy between cores.

4.3. Geochemical Composition of the Fåvne Deposits

4.3.1. Rock Samples

For geochemical results, all means are reported with one standarddeviation (1σ). All samples collected at Fåvne aredominated by Fe, with an average concentration of 36 ± 11 wt.% (n = 25), except for one Si-rich sample (>30 wt.%; Table 2) collected in the graben downslope from the North Tower vent. Other base metals are present at much lower concentrations and subject to associated large range of values (e.g., Zn: 3.1 ± 6.0 wt.%, Cu: 0.6 ± 1.4 wt.%, Pb: 56 ± 88 ppm; Figure 7). The sulfide-dominated interior of chimneys contains relatively high abundances of Zn, Cu, Pb, Co, Ag, Al, and Ca compared to Fe oxyhydroxide rich exteriors, which contain higher abundances of Fe, Si, Mn, Mo, As, Na, and Mg (Table 2, Figure 7). Barium concentrations are all <150 ppm. Overall, reported base and precious metal concentrations are significantly lower than those reported by Sahlström et al. (2023). This difference reflects the targeted analysis by Sahlström et al. (2023) of chimney fragments from high-temperature vents, whereas this study incorporates a data set more representative of the overall style of high- and low-temperature venting at Fåvne.

Within the sulfide-rich samples, average (non-Fe) base metal concentrations are highest for Zn (5.5 ± 7.2 wt.%), followed by Cu (1.0 ± 1.8 wt.%), Co (0.1 ± 0.1 wt.%), and Pb (96 ± 100 ppm; n = 14 for all base metals, Table 2; Table S2). Active chimneys have higher concentrations of Cu, Co, Ca, Sr, and Zn relative to inactive chimneys, which have higher concentrations of Fe, Si, Mo, Al, Na, and V. Samples have a wide range of Si concentrations, from 0.02 to >30 wt.%. Average Au concentration in the sulfide-rich samples is 356 ± 546 ppb (n = 14). The elemental composition of the Fe oxyhydroxide-rich samples is dominated by Fe, Si, and Mn (Table 2, Figure 7).

Figure 6. Iron oxyhydroxide-rich (a) and sulfide- and sulfate-rich (b) rock samples. (c) Iron oxyhydroxide-rich sample with filaments perpendicular to the opal layer. Photomicrographs of mineral textures and assemblages in reflected light (d–l). (d) Euhedral pyrrhotite, sphalerite, and chalcopyrite surrounding a conduit. (e) Pyrrhotite, pyrite, and magnetite forming curved, parallel structures, infilled with Fe oxyhydroxides. (f) Skeletal magnetite emanating from agglomerates of globular sphalerite, disseminated euhedral pyrite, and rare concentric chalcopyrite. (g) Fe oxyhydroxide and silica globules, with interspersed sphalerite grains. (h) Hexagonal pyrrhotite replacing sphalerite, and magnetite replacement lining sulfide minerals. (i) Curved successions of flared pyrrhotite and sphalerite. (j) Sphalerite replacing subhedral galena and euhedral pyrite. (k) Oxidized pyrrhotite, chalcopyrite and isocubanite grains surrounded by sphalerite lining. (l) Framboidal and colloform pyrite and marcasite grains. Abbreviations from Warr (2021): Ccp—chalcopyrite, Gn—galena, Icb—isocubanite, Mag—magnetite, Mrc—marcasite, Fe-ox—iron-oxyhydroxide, Py—pyrite, Po—pyrrhotite, Sp—sphalerite.

Geochemistry, Geophysics, Geosystems

10.1029/2024GC011481

Table 2
Elemental Geochemistry of the Fåvne Sulfide- and Fe Oxyhydroxide-Rich Rocks and Sediment Layers

Samples	Element Unit	Cu wt.%	Zn wt.%	Pb ppm	Fe wt.%	S wt.%	Si wt.%	Mn wt.%	Ni ppm	Co ppm	Au ppb	Ag ppm	Al ppm	Ca wt.%	Ba ppm	∑REE[a] ppm	Prn/Ybn	Cen/Cen*	Eun/Eun*[b]	Fe/(Fe + Mn + Al)
Sulfide-rich rocks	**Method**	ICP-MS	INAA	ICP-MS	INAA	ICP-MS	ICP-MS	ICP-MS	ICP-MS	ICP-MS	INAA	INAA	ICP-OES	ICP-OES	ICP-MS					
	Detection limit	0.0002	0.005	0.8	0.01	0.01	0.01	0.0003	10	0.2	2	5	100	0.01	3					
GS19_ROV14_R05	MVF, The Fingers	0.0133	0.371	74.9	14.0	20.7	0.36	0.018	b.d.	355	b.d.	b.d.	100	19.70	8	0.1	–	–	–	0.998
GS19_ROV16_R02	MVF, North Tower	1.1500	8.21	82.5	18.4	>25	0.18	0.016	b.d.	1,820	75	26	300	14.60	14	0.2	–	–	–	0.998
GS19_ROV14_R04	MVF, Eastwatch	4.8800	0.756	3.4	22.3	>25	0.04	0.001	b.d.	3,080	268	b.d.	100	14.10	21	0.2	–	–	–	1.000
GS19_ROV11_R17	MVF, The Fingers	5.6800	0.661	11.4	44.0	>25	0.14	0.011	b.d.	>5,000	777	b.d.	200	3.47	4	0.3	–	–	–	0.999
GS19_ROV11_R15	MVF, North Tower	0.0825	9.62	301.0	31.2	20.8	4.05	0.056	30	374	b.d.	99	200	1.19	5	0.0	–	–	–	0.998
GS19_ROV11_R16	MVF, North Tower	0.2810	28.10	157.0	23.0	>25	1.50	0.006	b.d.	2,140	b.d.	b.d.	300	0.17	13	0.2	–	–	–	0.998
GS19_ROV11_R14	MVF, North Tower	0.0230	2.50	46.1	6.81	8.2	>30	0.004	b.d.	26	b.d.	b.d.	300	0.05	53	0	–	–	–	0.995
GS19_ROV11_R07	MVF, Eastwatch	0.2830	9.89	134.0	43.7	14.5	1.23	0.081	10	869	b.d.	b.d.	200	0.05	9	0.2	–	–	–	0.998
GS19_ROV11_R05	EVF	0.3320	6.50	103.0	46.4	18.3	1.62	0.050	b.d.	1,130	61	13	100	0.03	5	0.2	–	–	–	0.999
GS19_ROV15_R11	Fault scarp	1.0500	5.32	14.4	37.5	>25	0.43	0.002	20	2,430	741	b.d.	3,000	0.07	b.d.	1.0	–	–	–	0.992
GS19_ROV11_R18	Fault scarp	0.0269	5.54	324.0	43.3	>25	0.04	0.001	b.d.	436	b.d.	b.d.	200	0.03	b.d.	0.2	–	–	–	1.000
GS19_ROV15_R02	Gnitahei	0.0196	0.114	79.4	40.7	>25	0.02	0.001	b.d.	65.3	2,050	b.d.	100	0.05	4	0.1	–	–	–	1.000
GS19_ROV15_R03	Gnitahei	0.0077	0.041	10.7	40.5	>25	0.57	0.002	10	433	524	b.d.	2,800	0.04	b.d.	2.4	1.73	–	–	0.993
GS19_ROV15_R04	Gnitahei	0.0018	b.d.	1.6	35.2	>25	6.52	0.002	50	249	475	b.d.	19,400	0.05	b.d.	3.2	0.43	–	–	0.948
Average (n = 14)		1.0	5.5	96	32	22	3	0.02	12	1,315	356	12	1,950	3.8	11	0.6	1.08	–	–	0.99
Standard deviation		1.8	7.2	100	12	5	8	0.02	13	1,384	546	25	4,931	6.6	13	0.9	0.65	–	–	0.01
Fe oxyhydroxide-rich rocks	**Method**	ICP-MS	ICP-MS	ICP-MS	ICP-OES	n.a.	ICP-OES	ICP-OES	ICP-MS	ICP-MS	n.a.	ICP-MS	ICP-OES	ICP-OES	ICP-OES					
	Detection limit	0.001	0.003	5	0.007		0.005	0.0008	20	1		0.5	53	0.007	2					
GS19_ROV16_R01	MVF, South Tower	0.009	0.014	b.d.	37.3	n.a.	7.70	0.538	b.d.	18	n.a.	b.d.	790	0.700	62	4.6	1.50	0.55	1.58	0.984
GS19_ROV11_R12	MVF, Central Mound	0.019	0.032	b.d.	43.8	n.a.	4.22	0.480	20	17	n.a.	b.d.	1,060	0.772	82	4.6	1.68	0.36	–	0.987

Geochemistry, Geophysics, Geosystems

10.1029/2024GC011481

Table 2
Continued

Samples	Element Unit	Cu wt.%	Zn wt.%	Pb ppm	Fe wt.%	S wt.%	Si wt.%	Mn wt.%	Ni ppm	Co ppm	Au ppb	Ag ppm	Al ppm	Ca wt.%	Ba ppm	∑REE[a] ppm	Prn/ Ybn	Cen/ Cen*	Eun/ Eun*[b]	Fe/ (Fe + Mn + Al)
GS19_ROV11_R10	MVF, South Tower	0.010	0.049	6	45.7	n.a.	2.81	1.293	b.d.	44	n.a.	b.d.	530	0.307	37	0.9	–	1.13	–	0.971
GS19_ROV11_R11	MVF, South Tower	0.020	0.058	5	43.3	n.a.	3.57	0.163	b.d.	23	n.a.	b.d.	740	0.765	68	3.2	1.82	0.45	0.90	0.995
GS19_ROV11_R08	MVF, Eastwatch	0.003	0.022	8	42.6	n.a.	3.73	0.263	b.d.	5	n.a.	b.d.	950	1.051	131	6.8	2.49	0.42	6.27	0.992
GS19_ROV11_R09	MVF	0.193	0.058	6	42.4	n.a.	4.25	2.672	40	250	n.a.	b.d.	1,750	0.672	78	11.0	2.50	0.60	1.00	0.937
GS19_ROV11_R13	MVF	0.003	0.015	b.d.	40.7	n.a.	6.06	0.036	b.d.	3	n.a.	b.d.	260	0.343	45	0.4	–	–	–	0.998
GS19_ROV11_R03	EVF	0.020	0.069	7	40.1	n.a.	4.59	2.664	b.d.	32	n.a.	0.6	480	0.686	59	1.5	–	0.98	–	0.937
GS19_ROV11_R02	EVF	0.098	0.020	b.d.	32.0	n.a.	9.87	7.257	30	115	n.a.	b.d.	2,540	0.450	122	7.8	2.30	1.04	1.39	0.810
GS19_ROV11_R04	EVF	0.027	0.265	17	40.1	n.a.	5.78	0.356	20	51	n.a.	2	1,590	0.815	68	13.2	2.64	0.86	0.99	0.987
GS19_ROV15_R10	Fault scarp	0.002	b.d.	b.d.	50.4	n.a.	0.73	0.201	b.d.	3	n.a.	b.d.	850	0.443	31	1.9	2.26	0.27	–	0.994
Average (n = 11)		0.04	0.1	6	42	–	5	1.45	16	51	–	0	1,049	0.6	71	5.1	2.15	–	–	0.96
Standard deviation		0.06	0.1	4	4	–	2	2.05	10	70	–	1	635	0.2	30	4.0	0.40	–	–	0.05
Average Fåvne rocks (n = 25)		0.6	3.1	56	36	22	4	0.65	14	759	356	7	1,554	2.4	38	2.56	1.93			
Standard deviation Fåvne rocks		1.4	6.0	88	11	5	6	1.53	12	1,212	546	20	3,741	5.2	37	3.54	0.64			
Push core sediments[c]	**Radiocarbon ages**																			
ROV12 PC02 3.5–9 cm		0.1569	0.0820	9.4	34.91	0.419	8.8	0.07	9	87	–	0.5	4,300	0.49	131	7.4	4.60	0.94	0.84	0.986
ROV12 PC02 12.5–16 cm		1.0194	0.3092	57.4	23.08	0.663	14.0	0.05	30	101	–	1.0	34,000	0.66	316	40.7	4.20	1.09	1.09	0.870
ROV12 PC02 16–19.5 cm		0.5861	0.6436	61.3	29.73	0.371	11.0	0.05	31	153	–	0.2	22,200	0.56	138	22.1	2.76	1.01	1.67	0.929
ROV17 PC01 0–5 cm	3,870 ± 20	0.3556	0.1439	45.4	18.15	0.429	17.0	0.29	40	140	–	0.8	47,000	0.88	535	55.7	4.28	1.05	0.87	0.784
ROV17 PC01 10.5–12.5 cm		0.9100	0.5577	20.0	47.70	–	2.3	0.03	b.d.	752	140	4.0	1,800	0.20	20	3.0	4.34	0.89	3.85	0.996
ROV17 PC01 12.5–13.5 cm		2.0500	2.0226	45.0	47.60	–	1.4	0.06	b.d.	1,704	240	9.0	1,400	0.40	13	2.5	–	0.76	10.16	0.996
ROV17 PC02 0–3 cm		0.2237	0.1207	32.8	14.01	0.143	19.0	1.77	62	173	–	0.1	56,400	1.20	540	56.5	3.30	1.09	0.92	0.654

Geochemistry, Geophysics, Geosystems

10.1029/2024GC011481

Table 2
Continued

Samples	Element Unit	Cu wt.%	Zn wt.%	Pb ppm	Fe wt.%	S wt.%	Si wt.%	Mn wt.%	Ni ppm	Co ppm	Au ppb	Ag ppm	Al ppm	Ca wt.%	Ba ppm	∑REE[a] ppm	Prn/ Ybn	Cen/ Cen*	Eun/ Eun*[b]	Fe/ (Fe + Mn + Al)
ROV17 PC02 6.5–10 cm	4,550 ± 25	0.8797	0.2703	64.1	38.22	0.380	6.1	0.47	21	419	–	0.5	15,800	0.44	210	20.6	3.99	1.00	1.86	0.949
ROV17 PC02 20.5–22.5 cm		6.4600	0.4938	58.0	39.80	–	3.0	0.29	6	2542	1,100	5.0	7,400	0.40	84	14.2	5.20	0.84	2.79	0.975
ROV17 PC02 25.5–28.5 cm	5,710 ± 40	5.2700	0.2947	75.3	30.73	3.409	4.3	0.36	13	1,574	–	7.3	11,600	0.51	110	19.1	5.10	1.07	2.24	0.953
ROV17 PC03 15.5–18.5 cm		0.9871	0.1029	49.9	24.54	0.452	13.0	0.11	31	125	–	1.8	35,100	0.54	576	44.2	4.14	1.07	0.89	0.871
ROV17 PC03 18.5–20 cm		2.8194	0.1444	46.6	25.69	0.966	13.0	0.10	43	214	–	4.0	30,300	0.49	257	44.6	4.86	1.12	1.17	0.891
ROV17 PC03 24.5–25 cm		0.1688	0.0774	56.1	26.42	0.178	11.0	0.12	23	49	–	0.1	25,700	0.54	194	50.0	4.96	1.16	1.21	0.908
Average (n = 13)		1.7	0.4	48	31	1	10	0.29	24	618	493	3	22,538	0.6	240	29.3	4.31	–	–	0.90
Standard deviation		1.9	0.5	17	10	1	6	0.45	18	773	431	3	16,889	0.2	189	19.2	0.69	–	–	0.09

Note. ICP: Inductively coupled plasma, AES: atomic emission spectroscopy, MS: mass spectroscopy, OES: optical emission spectroscopy, INAA: instrumental neutron activation analysis. Below detection: b.d.; not analyzed: n.a.; no value: –; averages calculated with half detection limits when value is below detection. [a]No Ce, Eu, Y. [b]Values are not calculated, see main text. [c]Detection limits and analytical methods for sediment push core analyses available in Gartman et al. (2024).

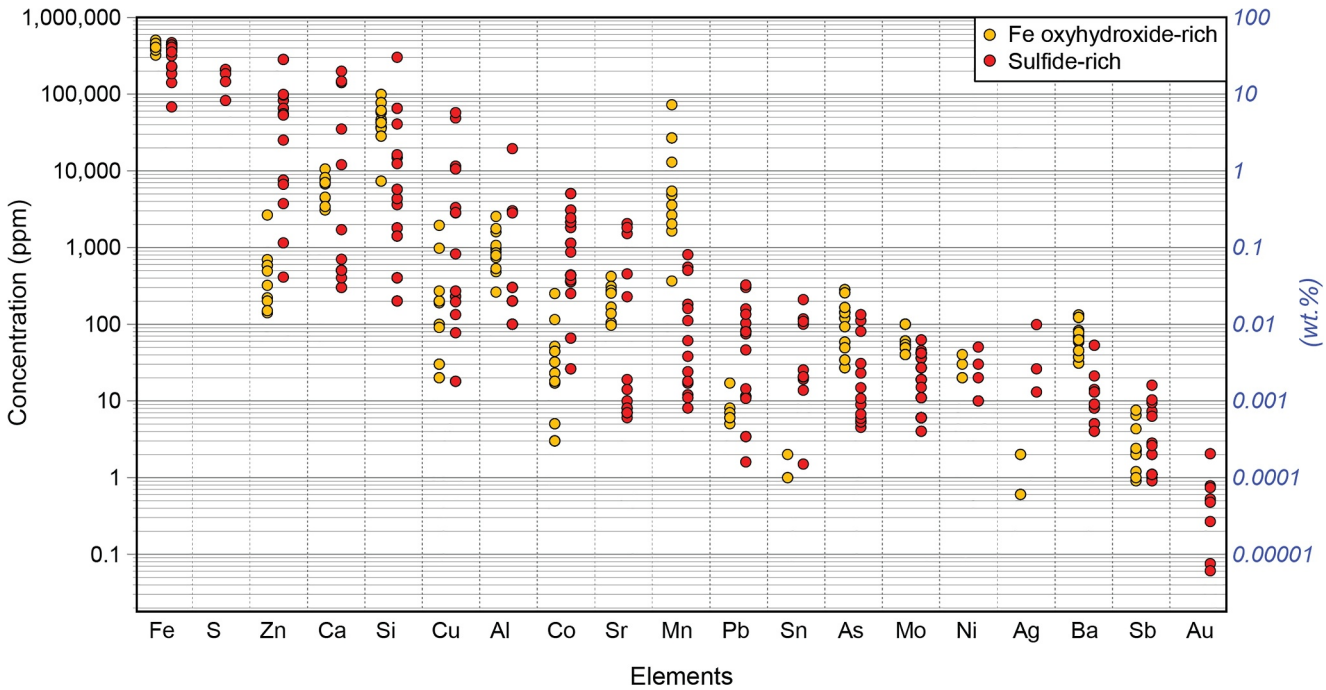

Figure 7. Elemental concentrations of Fe oxyhydroxide- and sulfide-rich samples displayed from highest to lowest average concentration in sulfide-rich samples. Concentrations below the detection limit are not displayed.

These samples are enriched in Mo and As, and depleted in Cu, Zn, Pb, Co, Ca, Sn, and Sr relative to the sulfide-rich samples.

The three sulfide-rich samples collected from the talus-covered footwall associated with Gnitahei have the highest Au concentration of this data set (1,016 ± 731 ppb; Table 2). Zinc (0.08 ± 0.04 wt.%) and Pb (30.6 ± 34.7 ppm) concentrations are similar to the low concentrations in the Fe oxyhydroxide-rich samples of the main field (0.01 ± 0.01 wt.% and 6 ± 4 ppm, respectively), whereas Cu concentrations (0.01 ± 0.01 wt.%) are the lowest overall of all samples in this data set.

Most rare earth element (REE) concentrations in the sulfide-rich samples are below analytical detection limits, except in two of the three samples associated with Gnitahei (Table S2). By contrast, the Fe oxyhydroxide-rich samples have measurable concentrations for most of the REEs, with an average sum of REEs (ΣREEs, calculated with all elements above detection limit but excluding anomalous REEs, i.e. Ce, Eu, Y) of 5.1 ± 4.0 ppm ($n = 11$), which is significantly higher than typical dissolved seawater concentrations reported from bottom water (e.g., 0.05 ± 0.004 ppm at the TAG hydrothermal vent field, Mid-Atlantic Ridge; Table 2; Figure S5 in Supporting Information S1; Mitra et al., 1994).

Chondrite-normalized (CN, McDonough & Sun, 1995) REE patterns for Fe oxyhydroxide-rich samples indicate an enrichment in light REE (LREE) relative to heavy REE (HREE), based on mean Pr_{CN}/Yb_{CN} of 2.15 ± 0.40 ($n = 8$; Table 2; Figure S5 in Supporting Information S1). Cerium (Ce_{CN}/Ce_{CN}^*) and Eu (Eu_{CN}/Eu_{CN}^*) anomalies (<0.85 or >1.15) were calculated using the geometric mean projection from Lawrence et al. (2006), where $Ce_{CN}^* = Pr_{CN}^*(Pr_{CN}/Nd_{CN})$ and $Eu_{CN}^* = Sm_{CN}^*(Sm_{CN}/Nd_{CN})^{1/2}$. For samples where analytical scatter influences the final anomaly calculation, the results are not reported in Table 2 or considered in the text. Six of the Fe oxyhydroxide-rich samples have a negative Ce anomaly (ranging from 0.27 to 0.60), while the other four Fe oxyhydroxide-rich samples have no analytically discernible Ce anomaly (Table 2). Iron oxyhydroxide-rich samples typically have a negligible Eu anomaly (0.90–1.00, $n = 3$), with the exception of three samples with a positive anomaly (1.39–6.27, $n = 3$), with the most positive Eu anomaly from a sample collected from a hydrothermally active edifice. The low REE concentrations in the sulfide-rich samples prevent the representation of REE patterns and calculation of Eu and Ce anomalies (Figure S5 in Supporting Information S1).

4.3.2. Push Core Sediments

All analyzed sediment layers from the push cores are composed primarily of Fe (average 31 ± 10 wt.%), Si (9.5 ± 5.5 wt.%), Al (2.3 ± 1.7 wt.%), and Na (1.6 ± 0.3 wt.%, $n = 13$; Table 2). Sediment layers are also enriched in LREE relative to HREE ($Pr_{CN}/Yb_{CN} = 4.3 \pm 0.7$). The layers with sulfide minerals contain higher abundances of hydrothermally associated elements, such as Cu, Zn, Fe, Co, Ag, Cd, and Sn (Table 2). The four sediment layers that contain sulfide minerals have the lowest Ce values (0.76–1.07, $n = 4$) from which only two samples have negative Ce anomalies ranging from 0.76 to 0.83, while the nine sediment layers without sulfide minerals have no analytically discernible Ce anomaly (Table 2). By contrast, sediment layers with sulfide minerals have a strong positive Eu anomaly (2.24–10.16, $n = 4$) and layers without sulfide minerals have both positive anomalies (1.17–1.86, $n = 3$) or no analytically discernible anomaly (Table 2). The sediment cores contain the highest concentrations of REEs amongst all samples collected at Fåvne, with average ΣREE of 29.3 ± 19.2 ppm ($n = 13$; Table 2). The ΣREE concentrations of both Fe oxyhydroxide and sediment layers are 1–2 orders of magnitude higher than the concentrations reported for sulfide mineralization at Fåvne (0.6 ± 0.9 ppm) and at other MOR-hosted vent fields, which have total concentrations that typically range from 0.1 to 1 ppm (Zeng et al., 2015).

Calculations of Fe/(Fe + Mn + Al) are used as a proxy to discriminate between pelagic (characterized by high Al) and hydrothermal (characterized by high Fe and Mn) origin of the sediments, with a value of >0.5 indicating dominantly hydrothermal origin, either from plume fall-out or mass wasting of hydrothermal structures (Gurvich, 2006, and references therein). All sediment core subsamples analyzed in this study have Fe/(Fe + Mn + Al) values of at least 0.65, indicating a dominantly hydrothermal origin (Table 2). Radiocarbon ages ranged from 3,870 ± 20 years at a depth interval of 0–5 cm to 5,710 ± 40 years at a depth interval of 25.5–28.5 cm (Table 2 and Table S4).

5. Discussion

Globally, high-temperature (>~200°C) hydrothermal vent fields and associated deposits are typically dominated by sulfide-rich mineralization but also contain Fe oxyhydroxide mineralization (Hannington et al., 1995). Iron-oxyhydroxide-rich mineralization can form from two independent but not necessarily mutually exclusive processes: (a) secondary replacement of previously precipitated sulfide minerals from prolonged exposure to seawater; or (b) primary precipitation from generally low-temperature (<100°C) hydrothermal fluids and microbial processes (Alt, 1988; Bogdanov et al., 1997; Emerson & Moyer, 2002; Gartman et al., 2011; Puteanus et al., 1991; Sun et al., 2013). Iron oxyhydroxide-rich sulfide-poor vent fields have also been described at MORs, such as Lilliput (southern MAR; Dekov et al., 2010), Hatiba Mons (Red Sea; van der Zwan et al., 2023), and Troll Wall (near Jan Mayen; Johannessen et al., 2017), and on intraplate volcanoes (Kama'ehuakanaloa; Hekinian et al., 1993), back-arc basins (Valu Fa Ridge; Sun et al., 2013) and arc volcanoes (Coriolis Troughs; Iizasa et al., 1998). In all cases, these deposits dominantly host diffuse low-temperature venting, abundant microbial activity, and low abundance or absence of sulfide minerals, suggesting that primary precipitation from low-temperature fluids is the primary control on the mineralization. At Troll Wall, high temperature venting occurs but is spatially separated from the Fe oxyhydroxide deposits (Johannessen et al., 2017). The Fåvne vent field shares these low-temperature characteristics but is unique due to the presence of higher-temperature venting (>267°C) and minor sulfide mineralization intimately associated with dominant Fe oxyhydroxide deposition.

5.1. Low to Moderate Fluid Temperatures at Fåvne

The ROV-based visual surveys of the Fåvne vent field, combined with the mineralogical and geochemical analysis of the surficial grab samples and fluid temperature data, all point to a vent field dominated by relatively low-temperature venting. The mounds and chimneys are composed primarily of low-temperature (<~100°C) Fe oxyhydroxide minerals and microbial mats, and higher-temperature sulfide mineralization is restricted to only a few sites of active and formerly active focused venting characterized by the steep-sided chimney structures. The overall low-temperature mineralization is also reflected in the high average concentrations of elements associated with low-temperature oxyhydroxide mineralization (Fe, Mn, Si) and corresponding low average concentrations of elements associated with higher-temperature sulfide minerals (Cu, Pb, Zn, Au, Ag, As, Cd, Sb; Co is a notable exception, see Section 5.3), compared to average concentrations for mafic-hosted seafloor hydrothermal systems, which typically form chimneys and mounds dominated by sulfide minerals (Alt et al., 1987; Hannington et al., 1995; Tivey & Delaney, 1986).

The stable maximum measured vent fluid temperature of 267°C at Fåvne is well below the theoretical maximum fluid temperature possible at this depth (>400°C, based on the seawater boiling curve; Bischoff & Rosenbauer, 1984). Hence, subcritical phase separation (boiling) is therefore not a plausible cause of the loss of metals. It is also noticeably lower than typical black smoker temperature maxima at other slow—ultraslow settings on the MAR, such as Lucky Strike, Logatchev 1 and Azhadze 1 (352–364°C, Charlou et al., 2010), Rainbow (370°C, Seyfried et al., 2011) and the 5°S area (407°C, Haase et al., 2007). This lower temperature at Fåvne suggests that either the fluids never reached such higher temperatures or that the fluids cooled substantially before reaching the seafloor. The occurrence of very thick black smoke (Figure 5j) is, however, a characteristic more typical of vent fluids well above ∼300°C (German et al., 2022), given the strong temperature-dependent constraints on Fe mobility in hydrothermal fluids (Pester et al., 2011; Seewald & Seyfried, 1990), and suggests that substantial subseafloor fluid cooling has occurred. Regardless, the dominance of low-temperature focused and diffuse venting relative to very few higher-temperature conduits, and an overall wide range of lower venting temperatures across the vent field, implies that extensive and variable mixing with cold seawater in the sub-seafloor may have diluted and/or cooled much of the ascending hydrothermal fluid across large areas of the site.

Sub-seafloor mixing would result in not only a reduction in vent fluid temperature but also changes in the vent fluid pH and redox potential, triggering the precipitation of sulfide minerals in the subsurface. Significant subseafloor sulfide precipitation would trap S and the higher temperature metals, depleting the hydrothermal fluid in these elements prior to reaching the seafloor, increasing the fluid Fe/S, and promoting the precipitation of primary Fe oxide (magnetite, hematite) and oxyhydroxide (goethite, ferrihydrite, lepidocrocite) minerals at the seafloor (Figure 6; Isobe & Gondo, 2013). The extreme depletion in Ba and lack of any detectable barite within both the sulfide- and Fe oxyhydroxide-rich samples further suggest subseafloor mixing due to the very low solubility of barite in the presence of dissolved sulfate from infiltrated seawater (Jamieson et al., 2016; Seyfried et al., 2003).

The major axial-valley bounding normal fault likely provides the primary sub-seafloor permeability network for hydrothermal circulation at this site, similar to the spatial associations of venting with axial valley bounding faults at, for example, Endeavor (Delaney et al., 1992), TAG (Karson & Rona, 1990), and Semenov 4 (Pertsev et al., 2012). However, the secondary antithetic fault, and the numerous smaller faults and fissures identified within the vent field indicate the potential for additional permeability pathways that could enable significant subseafloor fluid mixing (Figure 3; Curewitz & Karson, 1997).

5.2. Precipitation of Fe Oxyhydroxide Minerals

5.2.1. Secondary Replacement of Sulfide Minerals

Secondary replacement of metal sulfide minerals occurs because the sulfide minerals are in thermodynamic disequilibrium with oxygenated seawater and will oxidize with increasing exposure to seawater over time (Gartman & Findlay, 2020). At Fåvne, the partial to full dissolution of pyrrhotite, sphalerite, and chalcopyrite or replacement of these minerals by secondary minerals (e.g., Fe oxyhydroxide for Fe-rich sulfide minerals and atacamite for Cu-rich sulfide minerals) indicates that Fe oxyhydroxide accumulation by secondary replacement of sulfide minerals occurs at this site (Figures 6f, 6h, and 6k; Hannington, 1993).

The rate of oxidation of sulfide minerals is influenced by a combination of factors, including sample mineralogy, grain size and crystallinity, porosity, and local physicochemical conditions such as temperature, pH, effects of galvanic interactions, and concentrations of oxidizing agents (e.g., O_2, Fe^{3+}; Boyd & Scott, 1999; Kirk Nordstrom, 1982; Moses et al., 1987). In general, chalcopyrite, pyrrhotite, and sphalerite appear to oxidize faster than pyrite and their relative abundances will decrease, resulting in pyrite becoming the dominant sulfide mineral in the oldest deposits where minerals are consistently exposed to seawater (Cherkashov, 2017; Fallon et al., 2017; Gartman et al., 2020; Knight et al., 2018). Replacement Fe oxyhydroxide products are common on the exteriors of active and inactive chimneys, whereas atacamite generally occurs only on old inactive structures (Hannington, 1993). For example, at Fåvne, dissolution and/or replacement of chalcopyrite, pyrrhotite, and sphalerite occur alongside abundant Fe oxyhydroxides within the samples collected from the main Fåvne vent field, whereas atacamite is generally absent in these samples. By contrast, the hydrothermally inactive sulfide-rich talus sampled from the fault scarp, including the samples collected downslope of Gnitahei, contain abundant atacamite but low total Cu and much lower abundances of chalcopyrite as well as low sphalerite and pyrrhotite. The presence of atacamite as a Cu sulfide weathering product and little to no original Cu sulfides suggest near complete oxidation. More rapid oxidation occurring in ambient seawater compared to the partly reduced fluids around the vent field

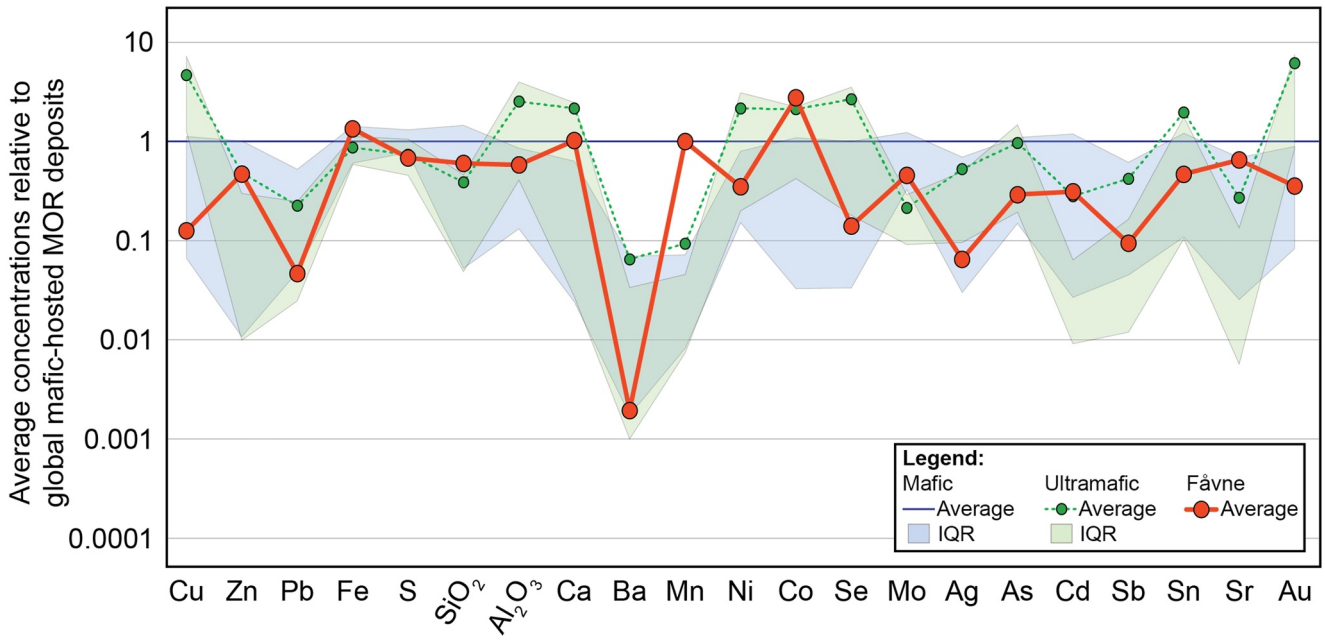

Figure 8. Comparison of the elemental concentrations of the Fåvne deposits (n = 25) and the global mid-ocean ridge average ultramafic hosted deposits (n = 110), relative to global average mafic hosted deposits (n = 1,440). Data from Hannington et al. (2004) and Toffolo et al. (2020), excluding sedimented ridges, miscellaneous and average values. Interquartile ranges (IQR) results are reported in Table S5.

may explain this observation; however, coupled to other lines of evidence, this may also suggest that the deposits that form the main Fåvne vent field are younger than the mineralization on the fault scarp, forming Gnitahei.

The radiocarbon ages from the sediment layers provide the only age constraint on hydrothermal activity at Fåvne and indicate a relatively young minimum age of ~5,710 years. However, the morphology of the vent deposits also indicates a young age for the field, consistent with the sediment radiocarbon ages. The oldest known vent fields along the MAR with ages of >100 Ka (e.g., Peterburgskoe, Pobeda, Semenov 4, Krasnov, TAG) are typically characterized by pyrite-rich mounds with diameters greater than 100 m that require prolonged periods of venting to form (Cherkashov et al., 2010, 2017; Jamieson et al., 2014; Kuznetsov et al., 2011; Lalou et al., 1990). By contrast, the relatively small size and close spacing of the hydrothermal edifices at Fåvne are similar to those of relatively young (<10 Ka) MOR-hosted vent fields, such as Lucky Strike (MAR) or Endeavor (Juan de Fuca Ridge; Jamieson et al., 2013; Sánchez-Mora et al., 2022).

The geological and mineralogical features summarized above to assess deposit age are, by themselves, not definitive, as deposit size and morphology are also affected by fluid flux, temperature, and mass accumulation rates (Jamieson et al., 2023). However, together, these observations suggest that Fåvne is relatively young, and dissolution or replacement of sulfide minerals alone cannot explain the high abundance of Fe oxyhydroxide minerals.

5.2.2. Primary Precipitation of Fe Oxyhydroxide Minerals

At Fåvne, the Fe oxyhydroxide-rich samples do not exhibit the same secondary-replacement textures that characterize Fe oxyhydroxide replacement minerals in the sulfide-rich samples. The Fe oxyhydroxide-rich samples are characterized by primary textures, such as filaments and microbial mats associated with abundant amorphous silica. Together, the Fe oxyhydroxide mineralogy, textures, and silica association indicate primary precipitation from a low-temperature (<~100°C) fluid venting (Hannington et al., 1995; Sun et al., 2013).

Microbial activity can play a significant role in the oxidation of Fe at low-temperature hydrothermal vents (Edwards, 2004; Emerson & Moyer, 2002). The abundance of filamentous textures within the Fe oxyhydroxide mineralization is indicative of significant microbially mediated precipitation and the occurrence of these textures at Fåvne has been linked to Fe-oxidizing Zetaproteobacteria (Hribovšek et al., 2023). These microbes oxidize reduced Fe in the hydrothermal fluid into poorly ordered ferrihydrite, forming complex mesh structures that

eventually transform into goethite (Figure 6c; Chan et al., 2011; Emerson & Moyer, 2002; Kennedy et al., 2004). Over time, microbial Fe-oxidation and construction of filamentous structures decrease the porosity of the deposit, isolating the hydrothermal fluid from surrounding seawater, and opal/amorphous Si precipitates as spherules or as layers along a saturation front due to conductive cooling (Figure 6c; Janecky & Seyfried, 1984; Sun et al., 2013; Yang et al., 2015). The high permeability of the chimney walls and resulting low-temperature environment, the abundance of diffuse venting, and the abundant reduced Fe in the fluid at Fåvne provide an ideal habitat for Fe-oxidizing microbes and associated precipitation of Fe oxyhydroxide mineralization (Boonnawa et al., 2022; Hribovšek et al., 2023). The visually estimated porosities in the high-temperature samples (~20%–40%) are much higher than those reported from high-temperature black smoker inner conduits (<5%–10%) at other sites due to the general absence of chalcopyrite conduit linings (Tivey, 1995; Tivey & McDuff, 1990; Tivey et al., 1995). A temperature of 50°C was measured in the ~cm thick Fe-oxidizing microbial biofilms on the exterior of North Tower vent (Hribovšek et al., 2023) compared to a maximum of 228°C measured at this vent orifice. This supports substantial fluid leakage of hydrothermal fluids through the chimney walls due to a high degree of permeability not commonly seen elsewhere, where much lower exterior temperatures are typically measured (e.g., ~2–30°C; Schrenk et al., 2003).

The higher ΣREE concentrations in the Fe oxyhydroxide-rich samples and sediment layers reflect the high absorption capacity associated with the large surface area of Fe oxyhydroxide minerals (Olivarez & Owen, 1989). The incomplete REE patterns and absence of coupled Y-Ho data in most samples due to concentrations below detection limits prevent a more in-depth assessment of fluid sources, mixing, and scavenging processes (e.g., Bau & Dulski, 1999). The two prominent REE anomaly features of the collective samples are the positive Eu anomaly preserved in sulfide-rich samples and one Fe oxyhydroxide-rich sample and the prominent negative Ce anomaly in the Fe oxyhydroxide-rich samples (Table 2). Positive Eu anomalies are generated in high-temperature hydrothermal fluids (Hekinian et al., 1993; Mitra et al., 1994) and suggest that even at low-temperature venting sites, some fluids may have originated as higher-temperature fluids. Dissolution of anhydrite may also contribute to a positive Eu anomaly in hydrothermal fluids in low-temperature fluid venting environments (James & Elderfield, 1996). By contrast, hydrothermal fluids are devoid of Ce anomalies, but strongly negative Ce anomalies are typical of oxygenated seawater (e.g., Alibo & Nozaki, 1999; Mitra et al., 1994). The presence of negative Ce anomalies provides an indication that Fe oxyhydroxides precipitated from fluid with a seawater component and/or scavenged soluble REE from seawater after formation.

5.3. Possible Influence of Ultramafic Substrate

A comparison of the bulk chemistry of the sulfide-rich and Fe oxyhydroxide-rich samples to global MOR average elemental concentrations highlights some unique geochemical aspects of the Fåvne vent field. Relative enrichment of Fe and Mn, and depletions of Cu, Pb, Zn, S, and Ba can be attributed to potential sub-seafloor mixing of the ascending hydrothermal fluid with local seawater and consequent precipitation of high-temperature sulfide minerals at depth (Figure 8, Table S5). Relative enrichment of Co in the sulfide-rich samples is the notable exception to this trend.

Cobalt enrichment in hydrothermal deposits is commonly associated with ultramafic influenced hydrothermal systems (Fouquet et al., 2010; German & Von Damm, 2006; Hannington et al., 2005; Liao et al., 2022; Marques et al., 2006). Sahlström et al. (2023) proposed that the elevated Co concentration at Fåvne is linked to high salinity fluids and suggested a possibility of an ultramafic influence at depth, but also noted the lack of other ultramafic fingerprinting element enrichment (Ni, Se, Sn). Similarly, in our data set, enrichment in other trace elements typically associated with ultramafic influence are absent (Figure 8). Interactions with an ultramafic substrate remain a possible source for high Co concentrations, but it is unclear why Ni and other ultramafic indicators are not similarly enriched. It is possible that subseafloor mixing with seawater may not have the same effect on Co as it has on the other base metals and ultramafic-associated elements. Cobalt enrichment relative to Ni has been attributed to temperature- and sulfur fugacity-dependent solubility differences, with Co being more soluble than Ni at high temperature (>300°C) and low sulfur fugacity, resulting in possible Ni deposition associated with subseafloor fluid mixing (Marques et al., 2007; Maslennikov et al., 2017; Meng et al., 2020; Sahlström et al., 2023). In general, our understanding of the mobility of trace metals such as Ni in seafloor hydrothermal fluids is limited relative to other metals present in higher abundances, such as Fe, Mn, Cu, and Zn, which are more commonly measured in fluids. Follow-up studies of vent fluid chemical compositions at Fåvne should provide

10.1029/2024GC011481

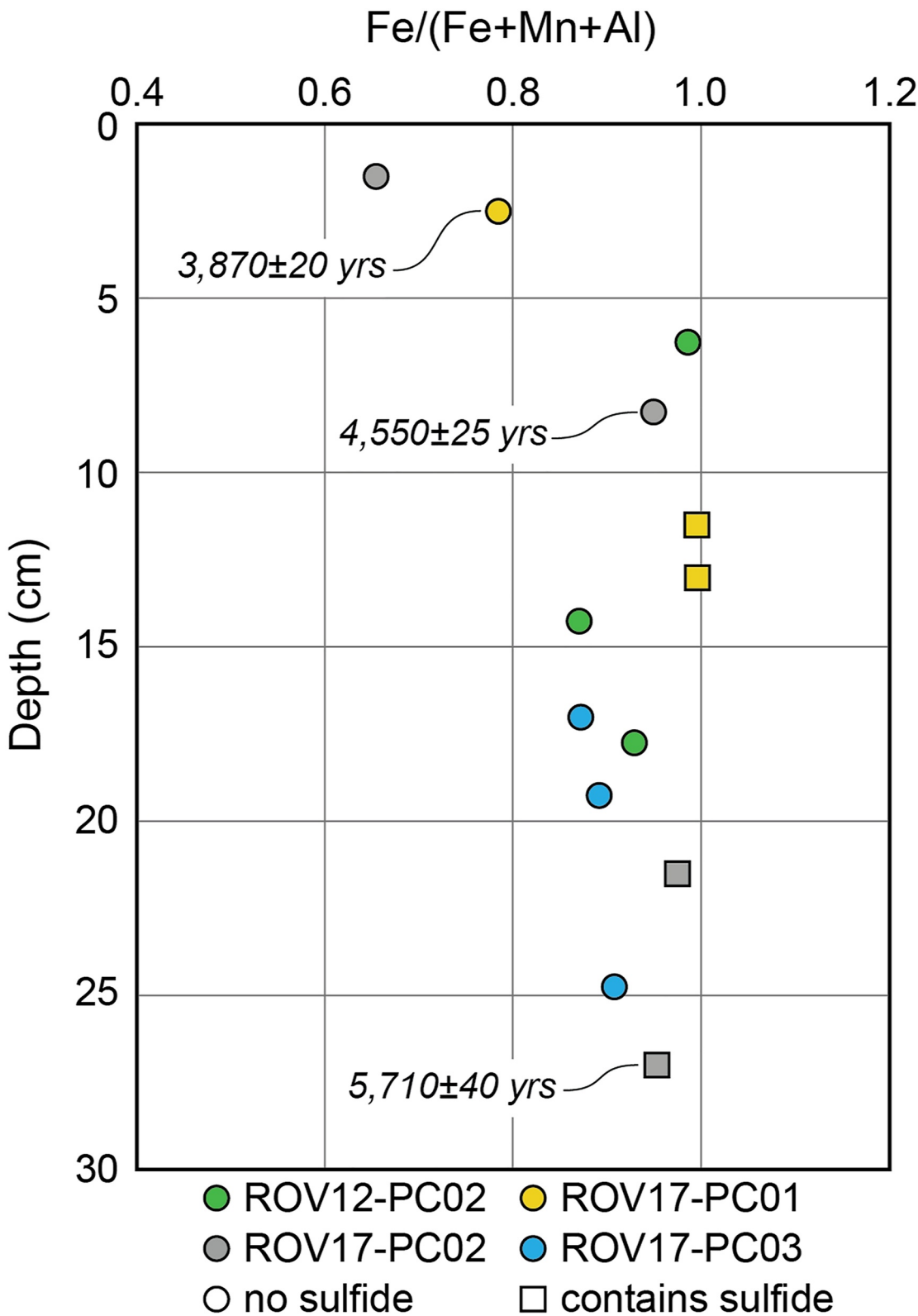

Figure 9. Sediment discrimination plot using Fe/(Fe + Mn + Al) ratio from Gurvich (2006) relative to depth of sediment. Radiocarbon ages are reported.

further insights into fluid salinity and the possibility of interactions with ultramafic substrates in the subsurface (Boonnawa et al., 2022).

5.4. Hydrothermal Sediments at Fåvne

The dominance of the hydrothermal component to the Fåvne sediments, as indicated by Fe/(Fe + Mn + Al) of >0.65, is consistent with the close proximity of the push cores to the hydrothermal edifices (~10 m; Figures 3 and 9). In addition, the four samples documented as having sulfide also have the strongest positive Eu anomalies (>2.0, Table 2), which are linked to sediments with a more directly captured hydrothermal origin (i.e., less modified by later adsorption of REE to oxyhydroxide precipitates). Data from the uppermost 5 cm of sediment (from cores GS19–ROV17–PC01 and GS19–ROV17–PC02; Figure 9) have distinctly lower Fe/(Fe + Mn + Al), indicating a recent decrease in hydrothermal contribution to sedimentation within the vent field. This decrease could be the result of either decrease of overall intensity of venting, changing in venting location, or shift in current direction. The close spatial clustering of the push cores within one part of the vent field impedes the determination of whether the sedimentation changes are local or occurred over the entire vent field. The majority of the sediment in the cores is represented by oxyhydroxide minerals that have accreted through mass wasting processes, which is consistent with the dominant mineralogy of the vent field as well as the location of the cores in a bathymetric low surrounded by chimneys and mounds. The recrystallization of ferrihydrite to goethite with depth in the core as well as the presence of crusty oxyhydroxide lamina within the cores (Gartman et al., 2024) suggest that significant post-depositional mobility and recrystallization occurs within the sediments.

Rates of sediment accumulation calculated based on the three radiocarbon ages ranged from 1.3 to 4.7 cm/ka (Figure 9). Since these layers all contain hydrothermal input, the radiocarbon ages represent maximum ages, as it cannot be ruled out that the incorporation of potentially radiocarbon-depleted hydrothermal material would result in artificially high calculated ages. The volcanic ash layers intercalated between the hydrothermal layers (GS19–ROV17–PC03, Figure S1 in Supporting Information S1) indicate that volcanic activity has occurred during the period of hydrothermal activity at Fåvne.

5.5. Mineral Resource Implications

From a mineral resource perspective, the surface expression of the Fåvne vent field is relatively small and contains low grades of economically interesting metals (Cu, Zn, Au, Ag; Hannington et al., 2010). The depth and grades of the metal accumulations below the seafloor at Fåvne are unknown, and current seafloor exploration and mining approaches are focused on surficial and shallow subseafloor deposits (Petersen et al., 2016). However, the site provides some insights into ore forming processes that are applicable to exploration for both SMS deposits on the modern ocean floor and land-based VMS deposits. Replacement style mineralization, commonly associated with high-permeability substrates, as proposed for Fåvne, promotes a high degree of sub-seafloor metal retention relative to surface mineralization, where metals are lost to the overlying ocean due to high-temperature venting or through secondary oxidation (Nozaki et al., 2021; Piercey, 2015). Therefore, vent fields characterized by low-temperature venting at the seafloor but with indications of high-temperature fluids at depth could be used as exploration vectors for sub-seafloor massive sulfide accumulations. Similarly, the location of the vent field within a fractured, and therefore potentially high permeability substrate associated with a major fault zone indicates that other submarine hydrothermal vent fields associated with similar large tectonic structures may also be less prospective at the surface. However, this type of geological setting would be prospective for land-based VMS exploration, where exploration is not limited to the (paleo)seafloor.

It is difficult to assess the resource potential of Gnitahei based on the three samples collected from the talus downslope of the site. These samples are enriched in Au but depleted in base metals relative to sulfide-rich samples from Fåvne. However, the low abundance of chalcopyrite and sphalerite, high abundance of atacamite, marcasite, and pyrite (which is likely the primary host of Au; Figure S4 in Supporting Information S1) all point to significant alteration of the primary mineralization due to oxidation associated with prolonged exposure at the seafloor. Further exploration and sampling are required to determine whether these three samples are representative of the Gnitahei deposit.

6. Conclusions

The dominantly moderate- to low-temperature mineralization and depletion of metals associated with high-temperature sulfide mineralization that characterize the Fåvne vent field are consistent with hydrothermal fluids that have been modified by cooling and/or mixing in the subseafloor prior to venting. The location of the vent field on a fractured substrate near a large-scale axial fault suggests that mixing of the ascending fluid with seawater that may have infiltrated the crust along permeability pathways generated by rifting along the ridge leads to fluid cooling and inferred subseafloor sulfide mineralization as well as widespread Fe oxyhydroxide deposition at the seafloor. Abundant moderate/low temperature fluid venting and the formation of porous sulfide chimneys with permeable conduit walls likely provide an energy-rich habitat for hydrothermal Fe-oxidizing microbial communities.

Hydrothermal sediments, which have accumulated in bathymetric lows around the vent field, exhibit similar composition and mineralogy to currently precipitating hydrothermal sulfides and oxyhydroxides, demonstrating a history of similar activity at Fåvne vent field as well as an eruption sequence. The sediment ages are consistent with the inferred relatively young age of the vent field.

The association of a high permeability substrate, metal-poor mineralization at the seafloor and associated metal-rich mineralization in the subsurface can be used as an exploration guide for both modern SMS deposits and ancient VMS deposits. The origin of the Co enrichment in the Fåvne deposits, in the absence of other ultramafic-associated metals or exposed ultramafic rocks at the seafloor, remains unclear.

Data Availability Statement

The push core data used for this study are available from Gartman et al. (2024) and all other data used in this study are freely available from the Zenodo (Gini et al., 2024; https://doi.org/10.5281/zenodo.11226438) online repository. All data are also included in the Supplementary Materials to this paper.

Acknowledgments
We thank the captain, crew, ROV *Ægir* technical team, and scientific party of the *G.O. Sars* CDeepSea summer 2019 cruise, which was supported by the University of Bergen through the Trond Mohn Foundation-funded *Centre for Deep Sea Research* (Grant TMS2020TMT13) and the Norwegian Petroleum Directorate. We thank Wanda Aylward for help with the XRD, EPMA, and SEM analyses. We thank Andrew Martin for constructive discussions during the preparation of the manuscript. This work was supported by funding from a Mitacs Accelerate Fellowship to CG (IT19515), a Canada Research Chair Grant to JJ (950-230933), the project *HyPOD* funded by the Research Council of Norway (Grant 287364), the Work Package 2 (Diversity & Functioning of Hydrothermal Systems) of the former K. G. Jebsen Centre for Deep Sea Research to ER, TB, SJ, and the U.S. Geological Survey Coastal and Marine Hazards and Resources Program through the U.S. Geological Survey Pacific Coastal and Marine Science Center to AG. Any use of trade, firm, or product names is for descriptive purposes only and does not imply endorsement by the U.S. Government. We thank Andrey Bekker for constructive review and Marie Edmonds for editorial handling.

References

Alibo, D. S., & Nozaki, Y. (1999). Rare Earth elements in seawater: Particle association, shale-normalization, and Ce oxidation. *Geochimica et Cosmochimica Acta*, *63*(3–4), 363–372. https://doi.org/10.1016/S0016-7037(98)00279-8

Alt, J. C. (1988). Hydrothermal oxide and nontronite deposits on seamounts in the eastern Pacific. *Marine Geology*, *81*(1–4), 227–239. https://doi.org/10.1016/0025-3227(88)90029-1

Alt, J. C., Lonsdale, P., Haymon, R., & Muehlenbachs, K. (1987). Hydrothermal sulfide and oxide deposits on seamounts near 21°N, East Pacific Rise. *Geological Society of America Bulletin*, *98*(2), 157. https://doi.org/10.1130/0016-7606(1987)98<157:HSAODO>2.0.CO;2

Bau, M., & Dulski, P. (1999). Comparing yttrium and rare Earths in hydrothermal fluids from the Mid-Atlantic Ridge: Implications for Y and REE behaviour during near-vent mixing and for the Y/Ho ratio of Proterozoic seawater. *Chemical Geology*, *155*(1–2), 77–90. https://doi.org/10.1016/S0009-2541(98)00142-9

Beaulieu, S. E., Baker, E. T., & German, C. R. (2015). Where are the undiscovered hydrothermal vents on oceanic spreading ridges? *Deep Sea Research Part II: Topical Studies in Oceanography*, *121*, 202–212. https://doi.org/10.1016/j.dsr2.2015.05.001

Beaulieu, S. E., & Szafrański, K. M. (2020). InterRidge global database of active submarine hydrothermal vent fields version 3.4 [WWW Document]. https://doi.org/10.1594/PANGAEA.917894

Bischoff, J. L., & Rosenbauer, R. J. (1984). The critical point and two-phase boundary of seawater, 200–500°C. *Earth and Planetary Science Letters*, *68*(1), 172–180. https://doi.org/10.1016/0012-821X(84)90149-3

Bogdanov, Y. A., Lisitzin, A. P., Binns, R. A., Gorshkov, A. I., Gurvich, E. G., Dritz, V. A., et al. (1997). Low-temperature hydrothermal deposits of Franklin Seamount, Woodlark Basin, Papua New Guinea. *Marine Geology*, *142*(1–4), 99–117. https://doi.org/10.1016/S0025-3227(97)00043-1

Bohrmann, G. (2022). Research cruise MSM109: 4thWeekly report.

Boonnawa, C., Viflot, T., Pereira, S., Barreyre, T., Jamieson, J. W., Stokke, R., et al. (2022). Diverse styles of hydrothermal chemistry on the ultraslow Arctic Mohns Ridge: The Fåvne, Ægir and Loki's Castle vent fields. In *AGU fall meeting abstracts* (p. OS55B-02).

Boyd, T., & Scott, S. D. (1999). Two-XRD-line ferrihydrite and Fe-Si-Mn oxyhydroxide mineralization from Franklin Seamount, western Woodlark Basin, Papua New Guinea. *The Canadian Mineralogist*, *37*, 973–990.

Brekke, H., Stenløkk, J., Eriksen, S. H., Bjørnstad, A., Sandstå, N. R., Solvi, K., & Schiager, P. (2021). Deep sea minerals on the Norwegian continental shelf—Developments in exploration. In *Proceedings of the 34th geological winter meeting, 6-8 January 2021 (virtual)* (pp. 1–48). Geological Society of Norway.

Chan, C. S., Fakra, S. C., Emerson, D., Fleming, E. J., & Edwards, K. J. (2011). Lithotrophic iron-oxidizing bacteria produce organic stalks to control mineral growth: Implications for biosignature formation. *ISME Journal*, *5*(4), 717–727. https://doi.org/10.1038/ismej.2010.173

Charlou, J. L., Donval, J. P., Konn, C., Ondréas, H., Fouquet, Y., Jean-Baptiste, P., & Fourré, E. (2010). High production and fluxes of H_2 and CH_4 and evidence of abiotic hydrocarbon synthesis by serpentinization in ultramafic-hosted hydrothermal systems on the Mid-Atlantic Ridge. In *Diversity of hydrothermal systems on slow spreading ocean ridges*, *Geophysical Monograph Series*. (pp. 265–296). https://doi.org/10.1029/2008GM000752

Chen, Y. J. (1992). Oceanic crustal thickness versus spreading rate. *Geophysical Research Letters*, *19*(8), 753–756. https://doi.org/10.1029/92GL00161

Cherkashov, G. (2017). Seafloor massive sulfide deposits: Distribution and prospecting. In R. Sharma (Ed.), *Deep-sea mining* (pp. 143–164). Springer International Publishing. https://doi.org/10.1007/978-3-319-52557-0_4

Cherkashov, G., Kuznetsov, V., Kuksa, K., Tabuns, E., Maksimov, F., & Bel'tenev, V. (2017). Sulfide geochronology along the northern equatorial Mid-Atlantic Ridge. *Ore Geology Reviews*, *87*, 147–154. https://doi.org/10.1016/j.oregeorev.2016.10.015

Cherkashov, G., Poroshina, I., Stepanova, T., Ivanov, V., Bel'tenev, V., Lazareva, L., et al. (2010). Seafloor massive sulfides from the northern equatorial Mid-Atlantic Ridge: New discoveries and perspectives. *Marine Georesources and Geotechnology*, *28*(3), 222–239. https://doi.org/10.1080/1064119X.2010.483308

Curewitz, D., & Karson, J. A. (1997). Structural settings of hydrothermal outflow: Fracture permeability maintained by fault propagation and interaction. *Journal of Volcanology and Geothermal Research*, *79*(3–4), 149–168. https://doi.org/10.1016/S0377-0273(97)00027-9

Dekov, V. M., Petersen, S., Garbe-Schönberg, C.-D., Kamenov, G. D., Perner, M., Kuzmann, E., & Schmidt, M. (2010). Fe–Si-oxyhydroxide deposits at a slow-spreading centre with thickened oceanic crust: The Lilliput hydrothermal field (9°33′S, Mid-Atlantic Ridge). *Chemical Geology*, *278*(3–4), 186–200. https://doi.org/10.1016/j.chemgeo.2010.09.012

Delaney, J. R., Robigou, V., McDuff, R. E., & Tivey, M. K. (1992). Geology of a vigorous hydrothermal system on the Endeavour Segment, Juan de Fuca Ridge. *Journal of Geophysical Research*, *97*(B13), 19663–19682. https://doi.org/10.1029/92JB00174

Dong, A., Sun, Z., Kendall, B., Izon, G., Cao, H., Li, Z., et al. (2022). Insights from modern diffuse-flow hydrothermal systems into the origin of post-GOE deep-water Fe-Si precipitates. *Geochimica et Cosmochimica Acta*, *317*, 1–17. https://doi.org/10.1016/j.gca.2021.10.001

Edwards, K. J. (2004). Formation and degradation of seafloor hydrothermal sulfide deposits. In *Sulfur biogeochemistry—Past and present* (pp. 83–96). Geological Society of America. https://doi.org/10.1130/0-8137-2379-5.83

Emerson, D., & Moyer, C. L. (2002). Neutrophilic Fe-oxidizing bacteria are abundant at the Loihi Seamount hydrothermal vents and play a major role in Fe oxide deposition. *Applied and Environmental Microbiology*, *68*(6), 3085–3093. https://doi.org/10.1128/AEM.68.6.3085-3093.2002

Escartín, J., Smith, D. K., Cann, J., Schouten, H., Langmuir, C. H., & Escrig, S. (2008). Central role of detachment faults in accretion of slow-spreading oceanic lithosphere. *Nature*, *455*(7214), 790–794. https://doi.org/10.1038/nature07333

Fallon, E. K., Petersen, S., Brooker, R. A., & Scott, T. B. (2017). Oxidative dissolution of hydrothermal mixed-sulphide ore: An assessment of current knowledge in relation to seafloor massive sulphide mining. *Ore Geology Reviews*, *86*, 309–337. https://doi.org/10.1016/j.oregeorev.2017.02.028

Fouquet, Y., Cambon, P., Etoubleau, J., Charlou, J. L., Ondréas, H., Barriga, F. J. A. S., et al. (2010). Geodiversity of hydrothermal processes along the Mid-Atlantic Ridge and ultramafic-hosted mineralization: A new type of oceanic Cu-Zn-Co-Au volcanogenic massive sulfide deposit. In *Diversity of hydrothermal systems on slow spreading ocean ridges* (pp. 321–367). American Geophysical Union. https://doi.org/10.1029/2008GM000746

Gartman, A., Au, M. V., & Payan, D. (2024). Computed tomography (CT) scans, photographs, X-ray fluorescence (XRF) scans, geochemistry, X-ray diffraction (XRD), and gamma-ray bulk density data of push cores from Loki's Castle and Favne vent fields, Mohns Ridge. https://doi.org/10.5066/P96D02FG

Gartman, A., & Findlay, A. J. (2020). Impacts of hydrothermal plume processes on oceanic metal cycles and transport. *Nature Geoscience*, *13*(6), 396–402. https://doi.org/10.1038/s41561-020-0579-0

Gartman, A., & Luther, G. W. (2014). Oxidation of synthesized sub-micron pyrite (FeS_2) in seawater. *Geochimica et Cosmochimica Acta*, *144*, 96–108. https://doi.org/10.1016/j.gca.2014.08.022

Gartman, A., Whisman, S. P., & Hein, J. R. (2020). Sphalerite oxidation in seawater with covellite: Implications for seafloor massive sulfide deposits and mine waste. *ACS Earth and Space Chemistry*, *4*(12), 2261–2269. https://doi.org/10.1021/acsearthspacechem.0c00177

Gartman, A., Yücel, M., Madison, A. S., Chu, D. W., Ma, S., Janzen, C. P., et al. (2011). Sulfide oxidation across diffuse flow zones of hydrothermal vents. *Aquatic Geochemistry*, *17*(4–5), 583–601. https://doi.org/10.1007/s10498-011-9136-1

Gates-Rector, S., & Blanton, T. (2019). The Powder Diffraction File: A quality materials characterization database. *Powder Diffraction*, *34*(4), 352–360. https://doi.org/10.1017/s0885715619000812

Géli, L., Renard, V., & Rommevaux, C. (1994). Ocean crust formation processes at very slow spreading centers: A model for the Mohns Ridge, near 72°N, based on magnetic, gravity, and seismic data. *Journal of Geophysical Research*, *99*(B2), 2995–3013. https://doi.org/10.1029/93jb02966

German, C. R., Reeves, E. P., Türke, A., Diehl, A., Albers, E., Bach, W., et al. (2022). Volcanically hosted venting with indications of ultramafic influence at Aurora hydrothermal field on Gakkel Ridge. *Nature Communications*, *13*(1), 6517. https://doi.org/10.1038/s41467-022-34014-0

German, C. R., & Von Damm, K. L. (2006). Hydrothermal processes. O Treatise, (Ed.)

Gini, C., Jamieson, J. W., Reeves, E. P., Gartman, A., Barreyre, T., Babechuk, M. G., et al. (2024). Data for: Iron oxyhydroxide rich hydrothermal deposits at the high-temperature Fåvne vent field, Mohns Ridge [Dataset]. In *Geochemistry, Geophysics, Geosystems*. Zenodo. https://doi.org/10.5281/zenodo.11226438

González, F. J., Rincón-Tomás, B., Somoza, L., Santofimia, E., Medialdea, T., Madureira, P., et al. (2020). Low-temperature, shallow-water hydrothermal vent mineralization following the recent submarine eruption of Tagoro volcano (El Hierro, Canary Islands). *Marine Geology*, *430*, 106333. https://doi.org/10.1016/j.margeo.2020.106333

Gurvich, E. G. (2006). *Metalliferous sediments of the world ocean*. Springer-Verlag. https://doi.org/10.1007/3-540-30969-1

Haase, K. M., Petersen, T., Koschinsky, A., Seifert, R., Devey, C. W., Keir, R., et al. (2007). Young volcanism and related hydrothermal activity at 5°S on the slow-spreading southern Mid-Atlantic Ridge. *Geochemistry, Geophysics, Geosystems*, *8*(11), Q11002. https://doi.org/10.1029/2006GC001509

Hannington, M., Jamieson, J., Monecke, T., & Petersen, S. (2010). Modern Sea-floor massive sulfides and base metal resources: Toward an estimate of global sea-floor massive sulfide potential. In *The challenge of finding new mineral Resources. Global metallogeny, innovative exploration, and new discoveries* (pp. 317–338). Society of Economic Geologists. https://doi.org/10.5382/SP.15.2.001

Hannington, M. D. (1993). The formation of atacamite during weathering of sulfides on the modern seafloor. *The Canadian Mineralogist*, *31*, 945–956.

Hannington, M. D., De Ronde, C. E. J., & Petersen, S. (2005). Sea-floor tectonics and submarine hydrothermal systems. In *One hundredth anniversary volume* (pp. 111–141). Society of Economic Geologists. https://doi.org/10.5382/AV100.06

Hannington, M. D., Jonasson, I. R., Herzig, P. M., & Petersen, S. (1995). Physical and chemical processes of seafloor mineralization at Mid-Ocean Ridges. In S. E. Humphris, R. A. Zierenberg, L. S. Mullineaux, & R. E. Thomson (Eds.), *Seafloor hydrothermal systems: Physical, chemical, biological, geological interactions* (pp. 115–157). American Geophysical Union. https://doi.org/10.1029/GM091p0115

Hannington, M. D., Petersen, S., Herzig, P. M., & Jonasson, I. R. (2004). A global database of seafloor hydrothermal systems, including a digital database of geochemical analyses of seafloor polymetallic sulfides. *Geological Survey of Canada Open File*, *4598*, 9. https://doi.org/10.4095/215065

Hekinian, R., Hoffert, M., Larque, P., Cheminee, J.-L., Stoffers, P., & Bideau, D. (1993). Hydrothermal Fe and Si oxyhydroxide deposits from South Pacific intraplate volcanoes and East Pacific Rise axial and off-axial regions. *Economic Geology*, *88*(8), 2099–2121. https://doi.org/10.2113/gsecongeo.88.8.2099

Hopkinson, L., Roberts, S., Herrington, R., & Wilkinson, J. (1998). Self-organization of submarine hydrothermal siliceous deposits: Evidence from the TAG hydrothermal mound, 26°N Mid-Atlantic Ridge. *Geology*, *26*(4), 347. https://doi.org/10.1130/0091-7613(1998)026<0347:SOOSHS>2.3.CO;2

Hribovšek, P., Olesin Denny, E., Dahle, H., Mall, A., Øfstegaard Viflot, T., Boonnawa, C., et al. (2023). Putative novel hydrogen- and iron-oxidizing sheath-producing Zetaproteobacteria thrive at the Fåvne deep-sea hydrothermal vent field. *mSystems*, *8*(6), e00543-23. https://doi.org/10.1128/msystems.00543-23

Humphris, S. E., Herzig, P. M., Miller, D. J., Alt, J. C., Becker, K., Brown, D., et al. (1995). The internal structure of an active sea-floor massive sulphide deposit. *Nature*, *377*(6551), 713–716. https://doi.org/10.1038/377713a0

Iizasa, K., Kawasaki, K., Maeda, K., Matsumoto, T., Saito, N., & Hirai, K. (1998). Hydrothermal sulfide-bearing Fe-Si oxyhydroxide deposits from the Coriolis Troughs, Vanuatu backarc, southwestern Pacific. *Marine Geology*, *145*(1–2), 1–21. https://doi.org/10.1016/S0025-3227(97)00112-6

Isobe, H., & Gondo, T. (2013). Dendritic magnetite crystals in rapid quenched fine spherules produced by falling experiments through the high temperature furnace with controlled gas flow. *Journal of Mineralogical and Petrological Sciences*, *108*(4), 227–237. https://doi.org/10.2465/jmps.121101

James, R. H., & Elderfield, H. (1996). Dissolved and particulate trace metals in hydrothermal plumes at the Mid-Atlantic Ridge. *Geophysical Research Letters*, *23*, 3499–3502. https://doi.org/10.1029/96gl01588

Jamieson, J. W., Clague, D. A., & Hannington, M. D. (2014). Hydrothermal sulfide accumulation along the Endeavour Segment, Juan de Fuca Ridge. *Earth and Planetary Science Letters*, *395*, 136–148. https://doi.org/10.1016/j.epsl.2014.03.035

Jamieson, J. W., Galley, C., McNeil, N., & Sánchez Mora, D. (2023). Evaluating episodicity of high-temperature venting within seafloor hydrothermal vent fields. *Earth and Planetary Science Letters*, *606*, 118051. https://doi.org/10.1016/j.epsl.2023.118051

Jamieson, J. W., Hannington, M. D., Clague, D. A., Kelley, D. S., Delaney, J. R., Holden, J. F., et al. (2013). Sulfide geochronology along the Endeavour Segment of the Juan de Fuca Ridge. *Geochemistry, Geophysics, Geosystems*, *14*(7), 2084–2099. https://doi.org/10.1002/ggge.20133

Jamieson, J. W., Hannington, M. D., Tivey, M. K., Hansteen, T., Williamson, N. M.-B., Stewart, M., et al. (2016). Precipitation and growth of barite within hydrothermal vent deposits from the Endeavour Segment, Juan de Fuca Ridge. *Geochimica et Cosmochimica Acta*, *173*, 64–85. https://doi.org/10.1016/j.gca.2015.10.021

Jamieson, J. W., Petersen, S., & Bach, W. (2015). Hydrothermalism. In J. Harff, M. Meschede, S. Petersen, & J. Thiede (Eds.), *Encyclopedia of marine geosciences* (pp. 1–20). Springer Netherlands. https://doi.org/10.1007/978-94-007-6644-0_15-1

Janecky, D. R., & Seyfried, W. E. (1984). Formation of massive sulfide deposits on oceanic ridge crests: Incremental reaction models for mixing between hydrothermal solutions and seawater. *Geochimica et Cosmochimica Acta*, *48*(12), 2723–2738. https://doi.org/10.1016/0016-7037(84)90319-3

Johannessen, K. C., Vander Roost, J., Dahle, H., Dundas, S. H., Pedersen, R. B., & Thorseth, I. H. (2017). Environmental controls on biomineralization and Fe-mound formation in a low-temperature hydrothermal system at the Jan Mayen Vent Fields. *Geochimica et Cosmochimica Acta*, *202*, 101–123. https://doi.org/10.1016/j.gca.2016.12.016

Karson, J. A., & Rona, P. A. (1990). Block-tilting, transfer faults, and structural control of magmatic and hydrothermal processesin the TAG area, Mid-Atlantic Ridge 26°N. *Geological Society of America Bulletin*, *102*(12), 1635–1645. https://doi.org/10.1130/0016-7606(1990)102<1635:BTTFAS>2.3.CO;2

Kennedy, C. B., Scott, S. D., & Ferris, F. G. (2004). Hydrothermal phase stabilization of 2-line ferrihydrite by bacteria. *Chemical Geology*, *212*(3–4), 269–277. https://doi.org/10.1016/j.chemgeo.2004.08.017

Kirk Nordstrom, D. (1982). Aqueous pyrite oxidation and the consequent formation of secondary iron minerals. In *Acid sulfate weathering* (pp. 37–56). SSSA Special Publications. https://doi.org/10.2136/sssaspecpub10.c3

Klingelhofer, F., Geli, L., Matias, L., Steinsland, N., & Mohr, J. (2000). Crustal structure of a super-slow spreading centre: A seismic refraction study of Mohns Ridge, 72N. *Geophysical Journal International*, *141*(2), 509–526. https://doi.org/10.1046/j.1365-246x.2000.00098.x

Knight, R. D., Roberts, S., & Cooper, M. J. (2018). Investigating monomineralic and polymineralic reactions during the oxidation of sulphide minerals in seawater: Implications for mining seafloor massive sulphide deposits. *Applied Geochemistry*, *90*, 63–74. https://doi.org/10.1016/j.apgeochem.2017.12.027

Kuznetsov, V., Maksimov, F., Zheleznov, A., Cherkashov, G., Bel'Tenev, V., & Lazareva, L. (2011). ^{230}Th/U chronology of ore formation within the semyenov hydrothermal district (13°31′N) at the Mid-Atlantic ridge. *Geochronometria*, *38*(1), 72–76. https://doi.org/10.2478/s13386-011-0001-1

Lalou, C., Thompson, G., Arnold, M., Brichet, E., Druffel, E., & Rona, P. A. (1990). Geochronology of TAG and Snakepit hydrothermal fields, Mid-Atlantic Ridge: Witness to a long and complex hydrothermal history. *Earth and Planetary Science Letters*, *97*(1–2), 113–128. https://doi.org/10.1016/0012-821X(90)90103-5

Lawrence, M. G., Greig, A., Collerson, K. D., & Kamber, B. S. (2006). Rare Earth element and yttrium variability in South East Queensland waterways. *Aquatic Geochemistry*, *12*(1), 39–72. https://doi.org/10.1007/s10498-005-4471-8

Liao, S., Tao, C., Jamieson, J. W., Liu, J., Zhu, C., Barriga, F. J. A. S., et al. (2022). Oxidizing fluids associated with detachment hosted hydrothermal systems: Example from the Suye hydrothermal field on the ultraslow-spreading southwest Indian Ridge. *Geochimica et Cosmochimica Acta*, *328*, 19–36. https://doi.org/10.1016/j.gca.2022.04.025

Little, C. T. S., Johannessen, K. C., Bengtson, S., Chan, C. S., Ivarsson, M., Slack, J. F., et al. (2021). A late Paleoproterozoic (1.74 Ga) deep-sea, low-temperature, iron-oxidizing microbial hydrothermal vent community from Arizona, USA. *Geobiology*, *19*(3), 228–249. https://doi.org/10.1111/gbi.12434

MacLeod, C. J., Searle, R. C., Murton, B. J., Casey, J. F., Mallows, C., Unsworth, S. C., et al. (2009). Life cycle of oceanic core complexes. *Earth and Planetary Science Letters*, *287*(3–4), 333–344. https://doi.org/10.1016/j.epsl.2009.08.016

Marques, A. F. A., Barriga, F., Chavagnac, V., & Fouquet, Y. (2006). Mineralogy, geochemistry, and Nd isotope composition of the Rainbow hydrothermal field, Mid-Atlantic Ridge. *Mineralium Deposita*, *41*(1), 52–67. https://doi.org/10.1007/s00126--005--0040--8

Marques, A. F. A., Barriga, F., & Scott, S. D. (2007). Sulfide mineralization in an ultramafic-rock hosted seafloor hydrothermal system: From serpentinization to the formation of Cu–Zn–(Co)-rich massive sulfides. *Marine Geology*, *245*(1–4), 20–39. https://doi.org/10.1016/j.margeo.2007.05.007

Maslennikov, V. V., Maslennikova, S. P., Large, R. R., Danyushevsky, L. V., Herrington, R. J., Ayupova, N. R., et al. (2017). Chimneys in Paleozoic massive sulfide mounds of the Urals VMS deposits: Mineral and trace element comparison with modern black, grey, white and clear smokers. *Ore Geology Reviews*, *85*, 64–106. https://doi.org/10.1016/j.oregeorev.2016.09.012

McDonough, W. F., & Sun, S.-S. (1995). The composition of the Earth. *Chemical Geology*, *120*(3–4), 223–253. https://doi.org/10.1016/0009-2541(94)00140-4

Meng, X., Li, X., Chu, F., Zhu, J., Lei, J., Li, Z., et al. (2020). Trace element and sulfur isotope compositions for pyrite across the mineralization zones of a sulfide chimney from the East Pacific Rise (1-2°S). *Ore Geology Reviews*, *116*, 103209. https://doi.org/10.1016/j.oregeorev.2019.103209

Mitra, A., Elderfield, H., & Greaves, M. (1994). Rare Earth elements in submarine hydrothermal fluids and plumes from the Mid-Atlantic Ridge. *Marine Chemistry*, *46*(3), 217–235. https://doi.org/10.1016/0304-4203(94)90079-5

Monecke, T., Petersen, S., Hannington, M. D., Grant, H., & Samson, I. M. (2016). The minor element endowment of modern sea-floor massive sulfides and comparison with deposits hosted in ancient volcanic successions. In *Rare Earth and critical elements in ore deposits* (pp. 245–306). Society of Economic Geologists. https://doi.org/10.5382/Rev.18.11

Moses, C. O., Kirk Nordstrom, D., Herman, J. S., & Mills, A. L. (1987). Aqueous pyrite oxidation by dissolved oxygen and by ferric iron. *Geochimica et Cosmochimica Acta*, *51*(6), 1561–1571. https://doi.org/10.1016/0016-7037(87)90337-1

Murton, B. J., Lehrmann, B., Dutrieux, A. M., Martins, S., de la Iglesia, A. G., Stobbs, I. J., et al. (2019). Geological fate of seafloor massive sulphides at the TAG hydrothermal field (Mid-Atlantic Ridge). *Ore Geology Reviews*, *107*, 903–925. https://doi.org/10.1016/j.oregeorev.2019.03.005

Norwegian Mapping Authority. (2019). Norwegian Mapping Authority, Hydrographic Service. Retrieved from dybdedata.kartverket.no

Norwegian Petroleum Directorate. (2019). Norwegian Petroleum Directorate, Stavanger, Norway. Retrieved from https://kartkatalog.geonorge.no/metadata/dyphavsundersoekelser-data/723af09b-cc8d-40eb-91a0-3a97093b83c9

Nozaki, T., Nagase, T., Takaya, Y., Yamasaki, T., Otake, T., Yonezu, K., et al. (2021). Subseafloor sulphide deposit formed by pumice replacement mineralisation. *Scientific Reports*, *11*(1), 8809. https://doi.org/10.1038/s41598-021-87050-z

Olivarez, A. M., & Owen, R. M. (1989). REE/Fe variations in hydrothermal sediments: Implications for the REE content of seawater. *Geochimica et Cosmochimica Acta*, *53*(3), 757–762. https://doi.org/10.1016/0016-7037(89)90019-7

Pedersen, R. B., Thorseth, I. H., Nygård, T. E., Lilley, M. D., & Kelley, D. S. (2010). Hydrothermal activity at the Arctic mid-ocean ridges. In P. Rona, C. W. Devey, J. Dyment, & B. Murton (Eds.), *Diversity of hydrothermal systems on slow spreading ocean ridges* (pp. 67–89). https://doi.org/10.1029/2008GM000783

Pertsev, A. N., Bortnikov, N. S., Vlasov, E. A., Beltenev, V. E., Dobretsova, I. G., & Ageeva, O. A. (2012). Recent massive sulfide deposits of the Semenov ore district, Mid-Atlantic Ridge, 13°31′N: Associated rocks of the oceanic core complex and their hydrothermal alteration. *Geology of Ore Deposits*, *54*(5), 334–346. https://doi.org/10.1134/S1075701512050030

Pester, N. J., Rough, M., Ding, K., & Seyfried, W. E. (2011). A new Fe/Mn geothermometer for hydrothermal systems: Implications for high-salinity fluids at 13°N on the East Pacific Rise. *Geochimica et Cosmochimica Acta*, *75*(24), 7881–7892. https://doi.org/10.1016/j.gca.2011.08.043

Petersen, S., Krätschell, A., Augustin, N., Jamieson, J., Hein, J. R., & Hannington, M. D. (2016). News from the seabed—Geological characteristics and resource potential of deep-sea mineral resources. *Marine Policy*, *70*, 175–187. https://doi.org/10.1016/j.marpol.2016.03.012

Peyve, A. A. (2009). Accretion of oceanic crust under conditions of oblique spreading. *Geotectonics*, *43*(2), 87–99. https://doi.org/10.1134/S0016852109020022

Piercey, S. J. (2015). A semipermeable interface model for the genesis of subseafloor replacement-type volcanogenic massive sulfide (VMS) deposits. *Economic Geology*, *110*(7), 1655–1660. https://doi.org/10.2113/econgeo.110.7.1655

Puteanus, D., Glasby, G. P., Stoffers, P., & Kunzendorf, H. (1991). Hydrothermal iron-rich deposits from the Teahitia-Mehitia and Macdonald hot spot areas, southwest Pacific. *Marine Geology*, *98*(2–4), 389–409. https://doi.org/10.1016/0025-3227(91)90112-H

Rouxel, O., Toner, B., Germain, Y., & Glazer, B. (2018). Geochemical and iron isotopic insights into hydrothermal iron oxyhydroxide deposit formation at Loihi Seamount. *Geochimica et Cosmochimica Acta*, *220*, 449–482. https://doi.org/10.1016/j.gca.2017.09.050

Sahlström, F., Strmić Palinkaš, S., Hjorth Dundas, S., Sendula, E., Cheng, Y., Wold, M., & Pedersen, R. B. (2023). Mineralogical distribution and genetic aspects of cobalt at the active Fåvne and Loki's Castle seafloor massive sulfide deposits, Arctic Mid-Ocean Ridges. *Ore Geology Reviews*, *153*, 105261. https://doi.org/10.1016/j.oregeorev.2022.105261

Sánchez-Mora, D., Jamieson, J., Cannat, M., Escartín, J., & Barreyre, T. (2022). Effects of substrate composition and subsurface fluid pathways on the geochemistry of seafloor hydrothermal deposits at the Lucky strike vent field, Mid-Atlantic Ridge. *Geochemistry, Geophysics, Geosystems*, *23*(5), e2021GC010073. https://doi.org/10.1029/2021GC010073

Schrenk, M. O., Kelley, D. S., Delaney, J. R., & Baross, J. A. (2003). Incidence and diversity of microorganisms within the walls of an active deep-sea sulfide chimney. *Applied and Environmental Microbiology*, *69*(6), 3580–3592. https://doi.org/10.1128/AEM.69.6.3580-3592.2003

Seewald, J. S., Doherty, K. W., Hammar, T. R., & Liberatore, S. P. (2002). A new gas-tight isobaric sampler for hydrothermal fluids. *Deep-Sea Research Part I Oceanographic Research Papers*, *49*(1), 189–196. https://doi.org/10.1016/S0967-0637(01)00046-2

Seewald, J. S., & Seyfried, W. E. (1990). The effect of temperature on metal mobility in subseafloor hydrothermal systems: Constraints from basalt alteration experiments. *Earth and Planetary Science Letters*, *101*(2–4), 388–403. https://doi.org/10.1016/0012-821X(90)90168-W

Seyfried, W. E., & Mottl, M. J. (1982). Hydrothermal alteration of basalt by seawater under seawater-dominated conditions. *Geochimica et Cosmochimica Acta*, *46*(6), 985–1002. https://doi.org/10.1016/0016-7037(82)90054-0

Seyfried, W. E., Pester, N. J., Ding, K., & Rough, M. (2011). Vent fluid chemistry of the Rainbow hydrothermal system (36°N, MAR): Phase equilibria and in situ pH controls on subseafloor alteration processes. *Geochimica et Cosmochimica Acta*, *75*(6), 1574–1593. https://doi.org/10.1016/j.gca.2011.01.001

Seyfried, W. E., Seewald, J. S., Berndt, M. E., Ding, K., & Foustoukos, D. I. (2003). Chemistry of hydrothermal vent fluids from the Main Endeavour Field, northern Juan de Fuca Ridge: Geochemical controls in the aftermath of June 1999 seismic events. *Journal of Geophysical Research*, *108*(B9), 2429. https://doi.org/10.1029/2002JB001957

Slack, J. F., Grenne, T., & Bekker, A. (2009). Seafloor-hydrothermal Si-Fe-Mn exhalites in the Pecos greenstone belt, New Mexico, and the redox state of ca. 1720 Ma deep seawater. *Geosphere*, *5*(3), 302–314. https://doi.org/10.1130/GES00220.1

Slack, J. F., Grenne, T., Bekker, A., Rouxel, O. J., & Lindberg, P. A. (2007). Suboxic deep seawater in the late Paleoproterozoic: Evidence from hematitic chert and iron formation related to seafloor-hydrothermal sulfide deposits, central Arizona, USA. *Earth and Planetary Science Letters*, *255*(1–2), 243–256. https://doi.org/10.1016/j.epsl.2006.12.018

Smith, D. K., Cann, J. R., & Escartín, J. (2006). Widespread active detachment faulting and core complex formation near 13°N on the Mid-Atlantic Ridge. *Nature*, *442*(7101), 440–443. https://doi.org/10.1038/nature04950

Stenløkk, J., Bering, D., Sandstå, N. R., Brekke, H., & Bjørnestad, A. (2019). The Norwegian Petroleum Directorate's seabed mapping of Fe-Mn crusts and massive sulphide deposits. In *Proceedings of the 33rd geological winter meeting*, 7–9 Januarzy 2019, Bergen, Norway (Vol. 1, p. 95). Geological Society of Norway.

Stensland, A., Baumberger, T., Mork, K. A., Lilley, M. D., Thorseth, I. H., & Pedersen, R. B. (2019). ^{3}He along the ultraslow spreading AMOR in the Norwegian-Greenland Seas. *Deep-Sea Research Part I Oceanographic Research Papers*, *147*, 1–11. https://doi.org/10.1016/j.dsr.2019.04.004

Stuiver, M. (1980). Workshop on ^{14}C data reporting. *Radiocarbon*, *22*(3), 964–966. https://doi.org/10.1017/S0033822200010389

Stuiver, M., & Polach, H. A. (1977). Discussion reporting of ^{14}C data. *Radiocarbon*, *19*(3), 355–363. https://doi.org/10.1017/S0033822200003672

Sun, Z., Zhou, H., Glasby, G. P., Sun, Z., Yang, Q., Yin, X., & Li, J. (2013). Mineralogical characterization and formation of Fe-Si oxyhydroxide deposits from modern seafloor hydrothermal vents. *American Mineralogist*, *98*(1), 85–97. https://doi.org/10.2138/am.2013.4147

Tivey, M. K. (1995). The influence of hydrothermal fluid composition and advection rates on black smoker chimney mineralogy: Insights from modeling transport and reaction. *Geochimica et Cosmochimica Acta*, *59*(10), 1933–1949. https://doi.org/10.1016/0016-7037(95)00118-2

Tivey, M. K., & Delaney, J. R. (1986). Growth of large sulfide structures on the endeavour segment of the Juan de Fuca ridge. *Earth and Planetary Science Letters*, *77*(3–4), 303–317. https://doi.org/10.1016/0012-821X(86)90142-1

Tivey, M. K., Humphris, S. E., Thompson, G., Hannington, M. D., & Rona, P. A. (1995). Deducing patterns of fluid flow and mixing within the TAG active hydrothermal mound using mineralogical and geochemical data. *Journal of Geophysical Research*, *100*(B7), 12527–12555. https://doi.org/10.1029/95JB00610

Tivey, M. K., & McDuff, R. E. (1990). Mineral precipitation in the walls of black smoker chimneys: A quantitative model of transport and chemical reaction. *Journal of Geophysical Research*, *95*(B8), 12617–12637. https://doi.org/10.1029/JB095iB08p12617

Toffolo, L., Nimis, P., Tret'yakov, G. A., Melekestseva, I. Y., & Beltenev, V. E. (2020). Seafloor massive sulfides from mid-ocean ridges: Exploring the causes of their geochemical variability with multivariate analysis. *Earth-Science Reviews*, *201*, 102958. https://doi.org/10.1016/j.earscirev.2019.102958

van der Zwan, F. M., Augustin, N., Petersen, S., Altalhi, S. M., Schultz, J., Peixoto, R. S., et al. (2023). Widespread diffuse venting and large microbial iron-mounds in the Red Sea. *Communications Earth & Environment*, *4*(1), 496. https://doi.org/10.1038/s43247-023-01169-7

Von Damm, K. L. (1990). Seafloor hydrothermal activity: Black smokers and chimneys. *Annual Review of Earth and Planetary Sciences*, *18*(1), 173–204. https://doi.org/10.1146/annurev.earth.18.1.173

Warr, L. N. (2021). IMA–CNMNC approved mineral symbols. *Mineralogical Magazine*, *85*, 291–320. https://doi.org/10.1180/mgm.2021.43

Yang, B., Zeng, Z., Qi, H., Wang, X., Ma, Y., & Rong, K. (2015). Constraints on biotic and abiotic role in the formation of Fe-Si oxides from the PACMANUS hydrothermal field. *Ocean Science Journal*, *50*(4), 751–761. https://doi.org/10.1007/s12601-015-0067-4

Zeng, Z., Ma, Y., Yin, X., Selby, D., Kong, F., & Chen, S. (2015). Factors affecting the rare Earth element compositions in massive sulfides from deep-sea hydrothermal systems. *Geochemistry, Geophysics, Geosystems*, *16*(8), 2679–2693. https://doi.org/10.1002/2015GC005812

Erratum

The originally published version of this article contained some errors in Figure 7. The y-axis label "(wt%)" should appear on the right-hand side of the plot and on the y-axis label on the right-hand side "1." should appear as "1" without the decimal point. The errors have been corrected, and this may be considered the authoritative version of record.